Resource

Developmental Cell

Dynamic changes in P300 enhancers and enhancer-promoter contacts control mouse cardiomyocyte maturation

Graphical abstract

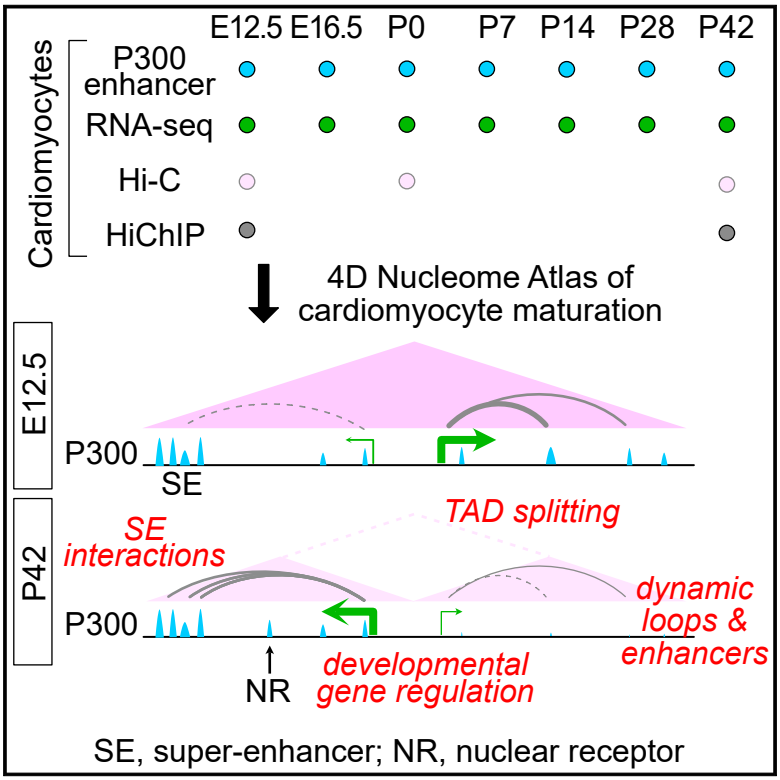

Highlights

- Developmental census of murine cardiomyocyte gene expression, enhancers, and 3D genomes
- Enhancer-chromatin conformation interactions regulate developmental cardiomyocyte genes
- Validation of developmentally regulated enhancers in maturing cardiomyocytes
- Nuclear receptor motifs are required for maturational enhancer activation

Authors

Pingzhu Zhou, Nathan J. VanDusen, Yanchun Zhang, ..., Bing Ren, Kaifu Chen, William T. Pu

Correspondence

kaifu.chen@childrens.harvard.edu (K.C.), william.pu@cardio.chboston.org (W.T.P.)

In brief

Many cell types undergo changes postnatally to acquire their specialized mature phenotypes, and the governing mechanisms are understudied. Here, Zhou et al. integrate cardiomyocyte-specific profiling of gene expressions, enhancers, and 3D genomes across murine development to identify interactions between dynamic enhancers and the changing 3D genomes regulating maturational gene expressions.

Zhou et al., 2023, Developmental Cell *58*, 1–17
May 22, 2023
https://doi.org/10.1016/j.devcel.2023.03.020

CellPress

Developmental Cell

CellPress

Resource

Dynamic changes in P300 enhancers and enhancer-promoter contacts control mouse cardiomyocyte maturation

Pingzhu Zhou,[1,11] Nathan J. VanDusen,[2,11] Yanchun Zhang,[1,11] Yangpo Cao,[1,11] Isha Sethi,[1] Rong Hu,[3] Shuo Zhang,[4] Guangyu Wang,[5] Lincai Ye,[6] Neil Mazumdar,[1] Jian Chen,[1] Xiaoran Zhang,[1] Yuxuan Guo,[7] Bin Li,[3] Qing Ma,[1] Julianna Y. Lee,[1] Weiliang Gu,[1,8] Guo-Cheng Yuan,[9] Bing Ren,[3] Kaifu Chen,[1,*] and William T. Pu[1,10,12,*]

[1]Department of Cardiology, Boston Children's Hospital, Boston, MA, USA
[2]Department of Pediatrics, Indiana University School of Medicine, Indianapolis, IN, USA
[3]Ludwig Institute for Cancer Research, Department of Cellular and Molecular Medicine, University of California, San Diego, La Jolla, CA, USA
[4]Houston Methodist Hospital Research Institute, Houston, TX 77030, USA
[5]Cardiovascular Department, Houston Methodist, Weill Cornell Medical College, Houston, TX, USA
[6]Department of Thoracic and Cardiovascular Surgery, Shanghai Children's Medical Center, School of Medicine, Shanghai Jiao Tong University, Shanghai, China
[7]Peking University Health Science Center, Beijing, China
[8]Department of Pharmacology, School of Pharmacy, Shanghai University of Traditional Chinese Medicine, Shanghai, China
[9]Department of Genetics and Genomic Sciences, Charles Bronfman Institute for Personalized Medicine, Icahn School of Medicine at Mount Sinai, New York, NY 10029, USA
[10]Harvard Stem Cell Institute, Cambridge, MA, USA
[11]These authors contributed equally
[12]Lead contact
*Correspondence: kaifu.chen@childrens.harvard.edu (K.C.), william.pu@cardio.chboston.org (W.T.P.)
https://doi.org/10.1016/j.devcel.2023.03.020

SUMMARY

Cardiomyocyte differentiation continues throughout murine gestation and into the postnatal period, driven by temporally regulated expression changes in the transcriptome. The mechanisms that regulate these developmental changes remain incompletely defined. Here, we used cardiomyocyte-specific ChIP-seq of the activate enhancer marker P300 to identify 54,920 cardiomyocyte enhancers at seven stages of murine heart development. These data were matched to cardiomyocyte gene expression profiles at the same stages and to Hi-C and H3K27ac HiChIP chromatin conformation data at fetal, neonatal, and adult stages. Regions with dynamic P300 occupancy exhibited developmentally regulated enhancer activity, as measured by massively parallel reporter assays in cardiomyocytes *in vivo*, and identified key transcription factor-binding motifs. These dynamic enhancers interacted with temporal changes of the 3D genome architecture to specify developmentally regulated cardiomyocyte gene expressions. Our work provides a 3D genome-mediated enhancer activity landscape of murine cardiomyocyte development.

INTRODUCTION

Coordinated changes in gene expressions, governed by epigenetic mechanisms including the transcriptional regulation by enhancers and three-dimensional (3D) chromatins,[1,2] drive cell differentiation. The developmental roles of enhancer activation and 3D genome organizations have been studied extensively in early embryogenesis and lineage specification from pluripotent stem cells (PSCs).[3,4] However, less is known about the later stages of embryonic and postnatal development, when cell lineages continue to differentiate to their mature state. Indeed, a few time courses of the 3D genome organization during fetal-to-adult maturation have been reported.

Cardiomyocytes (CMs) are specified from mesoderm between embryonic day (E)7.5–E10.5 of murine development and continue to differentiate throughout gestation. A dramatic change in the CM phenotype and transcriptome, CM maturation, occurs during the first postnatal week. CMs largely withdraw from the cell cycle, become reliant on oxidative phosphorylation, and switch expressions of several sarcomere gene isoforms.[5] Among the identified transcriptional regulators of CM maturation are serum response factor - myocardin-related transcription factor (SRF-MRTF),[6,7] thyroid hormone receptor alpha (THRA),[8] and peroxisome proliferator-activated receptor gamma coactivator 1 (PPARGC1A).[9] The enhancer network that governs CM differentiation and maturation remains incompletely defined. Moreover, studies of developmental changes in the CM 3D genome organization have been limited to differentiating PSCs,[10,11] which fail to mature.[5,12] As a result, we lack an understanding of the later developmental changes in the CM 3D genome and their contributions to maturation.

Please cite this article in press as: Zhou et al., Dynamic changes in P300 enhancers and enhancer-promoter contacts control mouse cardiomyocyte maturation, Developmental Cell (2023), https://doi.org/10.1016/j.devcel.2023.03.020

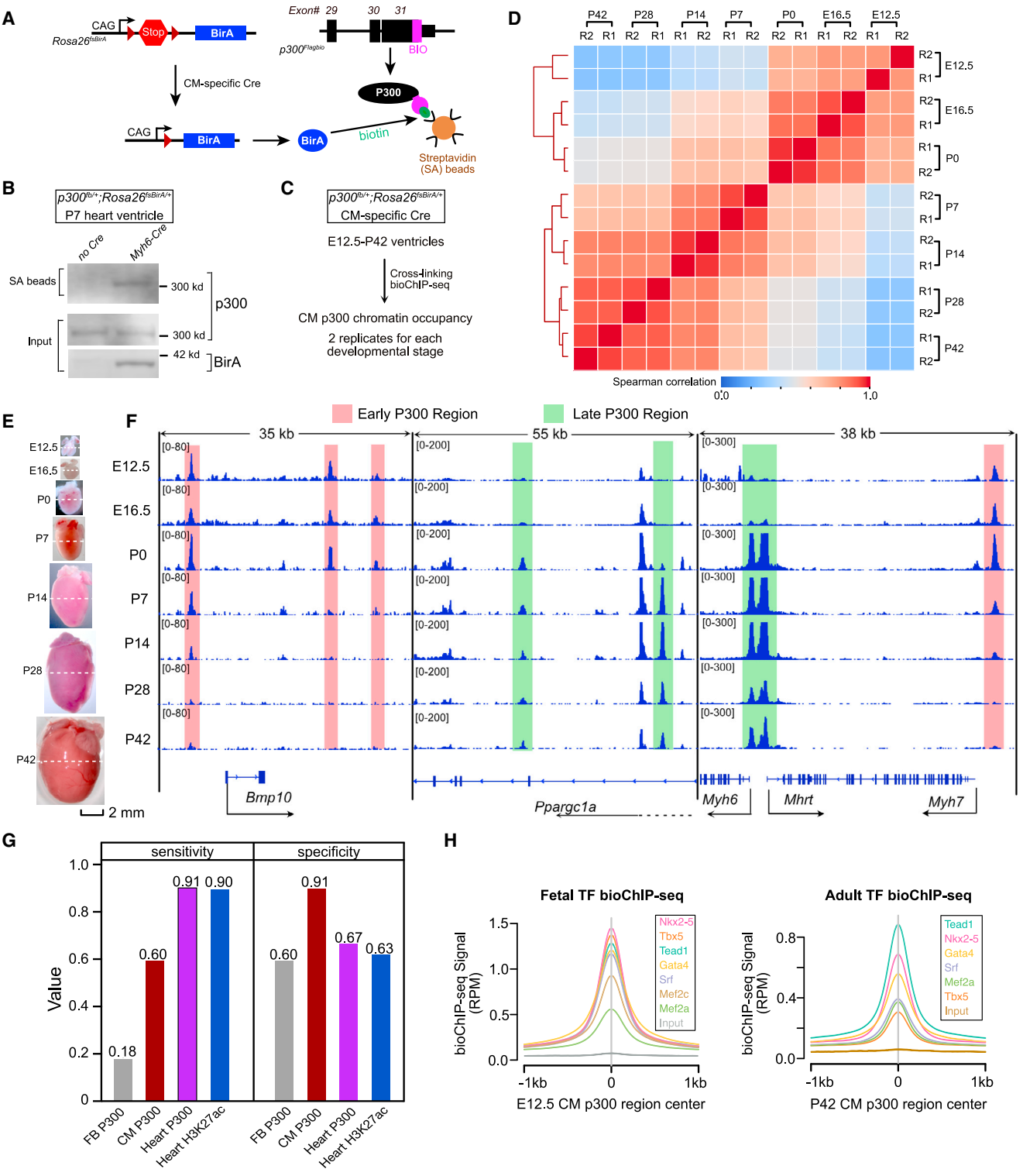

Figure 1. Identification of CM P300 enhancers

(A) Cre-dependent expression of BirA enabled CM-selective biotinylation of P300. The BIO tag was knocked into the C terminus of P300.

(B) P300 biotinylation was triggered by CM Cre expressions. Input: heart extracts. SA, streptavidin.

(C) P300 data acquisition.

(D) Spearman correlation of P300 signal across the union of P300 regions.

(E) Representative images of hearts used in this study, shown at the same scale. Ventricular tissue (below the dashed lines) was used.

(F) P300 bioChIP-seq signal at *Bmp10*, *Ppargc1a*, and *Myh6*/*Myh7*.

(legend continued on next page)

Please cite this article in press as: Zhou et al., Dynamic changes in P300 enhancers and enhancer-promoter contacts control mouse cardiomyocyte maturation, Developmental Cell (2023), https://doi.org/10.1016/j.devcel.2023.03.020

Dissection of gene regulatory mechanisms in developing tissues faces several challenges. One is the diversity of cell types in mammalian tissues and their changing distribution during development. For instance, the fraction of CMs in the heart decreases throughout development, dropping from ~80% at E11.5[13] to ~30%–35% in adult murine hearts.[14] Previous studies using chromatin immunoprecipitation followed by the next-generation sequencing (ChIP-seq) of transcription factors (TFs)[15] or active enhancer markers H3K27ac[16] and P300[17] successfully identified cardiac enhancers but did not account for cellular heterogeneity and the changing frequencies of CMs in developing hearts. High-throughput measurement of the enhancer activity of enhancers identified by their chromatin features is another challenge. Transient transgenesis is the gold standard approach, but it is slow and resource-intensive. As a result, less than 200 active murine cardiac enhancers have been identified by this method,[16,18] and their activity changes over time have not been systematically measured.

Here, we established a CM 4D-nucleome atlas of CM maturation that encompasses the CM-targeted measurement of gene expressions, P300 chromatin occupancy, *in vivo* enhancer activity, and 3D genome architectures between E12.5 through adulthood. Our integrative analysis identified mechanisms that regulate CM gene expressions through interactions between dynamic enhancers and 3D chromatin contacts.

RESULTS

The CM enhancer landscape during mouse development

We used a lineage-specific P300 bioChIP-seq system (Figure 1A) that enables highly sensitive and lineage-targeted identification of active enhancers from tissues and avoids the effects of cell dissociation on the chromatin state. We tagged endogenous P300, a transcriptional coactivator and a marker of active enhancers,[17] with C-terminal FLAG and BIO tags ($P300^{flbio}$).[19] The BIO sequence was selectively biotinylated by BirA,[20] a biotin ligase whose expression from a conditional allele ($Rosa26^{fsBirA}$; fs, flox-stop) was triggered by CM-specific Myh6-Cre.[19] Heart expressions of BirA and P300 biotinylation required Myh6-Cre (Figure 1B). We then compared the obtained heart bioChIP-seq data with the widespread expressions of BirA (Pan_P300: germline Cre activation[19]), CM-selective expressions (CM_P300: Myh6-Cre), and endothelium-selective expressions (EC_P300: CHD5-CreERT2[19]) (Figures S1A and S1B). Replicate experiments confirmed the high reproducibility of P300 bioChIP-seq and the differences in P300 chromatin occupancy between CM_P300, EC_P300, and Pan_P300 (Figures S1C–S1E). CM_P300, but not EC_P300, demonstrated strong P300 signal flanking CM-specific genes *Myl2*, *Ryr2*, and *Scn5a* (Figure S1D), whereas EC_P300, but not CM_P300, showed strong signal flanking endothelial cell-specific genes *Egfl7*, *Notch1*, and *S1pr1* (Figure S1E). Pan_P300 contained both CM and EC P300 signals (Figures S1D and S1E).

We targeted bioChIP-seq to CMs using either Tnnt2-Cre[21] (embryonic stages) or Myh6-Cre (postnatal stages) and measured P300 chromatin occupancy at seven developmental stages (E12.5, E16.5, P0, P7, P14, P28, and P42; P, postnatal day; Figures 1C–1E, S1F, and S1G; Data S1). Heart ventricles were sampled in biological duplicates (Figure S1H), which were highly correlated with one another (Figure 1D). In total, 54,920 P300-enriched regions were reproducible between replicates (see STAR Methods; Data S1). Most P300 regions were distal (>1 kb) to transcriptional start sites (TSSs; Figure S1H), consistent with previous studies.[17,19] Occupancy adjacent to developmentally regulated genes dynamically changed during development. For example, P300 occupancy of the regions flanking *Bmp10* (downregulated), *Ppargc1a* (upregulated), and *Myh6-Myh7* (downregulated and upregulated, respectively) genes coincided with their temporal expression patterns (Figure 1F).

To assess cardiac enhancer detection by CM-selective P300 bioChIP-seq, we used the Vista enhancer database,[18] which houses the results of thousands of regions tested for enhancer activity using the transient transgenic assay. Comparison groups were E12.5 heart ventricle Pan_P300,[19] heart ventricle H3K27ac,[19] and forebrain P300 bioChIP-seq.[19] Of the 1,372 murine regions in Vistas, 175 had heart activity. CM p300 bioChIP-seq identified 60% of these (Figure S1I) with high (91%) specificity (fraction of regions without heart activity that lacked P300 occupancy; Figure 1G). Pan_P300 and H3K27ac had greater sensitivity (fraction of regions with heart activity that had P300 occupancy; 91% and 90%) and reduced specificity (67% and 63%). As expected, forebrain P300 regions had lower sensitivity (18%) and specificity (60%) for heart enhancer activity. Vista heart enhancers bound by P300 in CMs were highly enriched for gene ontology (GO) terms related to heart and cardiac muscle development (Figure S1J), whereas without P300 in CMs, were related to blood vessel development (Figure S1K). Activity in non-CMs scored as heart enhancer activity in the Vista database likely depressed the calculated sensitivity of CM-selective p300 bioChIP-seq.

P300 occupies genomic DNA indirectly through interactions with DNA-binding TFs, including cardiac transcriptional regulators GATA binding protein 4 (GATA4), myocyte enhancer factor 2A (MEF2A), MEF2C, TEA domain family member 1 (TEAD1), Tbox transcription factor 5 (TBX5), SRF, and NKX2–5.[22–26] Fetal and adult genome-wide occupancy data for these TFs[15] showed that each TF is highly enriched at E12.5 and adult CM_P300 regions (Figure 1H). TBX5 was among the most highly enriched regulator at E12.5 but was the least enriched in adult samples, consistent with TBX5 downregulation in adult heart ventricles.

Dynamic landscape of active enhancers reveals key TFs that regulate CM differentiation

We focused on P300 regions with dynamic occupancy across the developmental time course. Filtering out low-signal peaks and peaks not found in at least two time points left 43,063 regions, which we ranked by the ratio of each region's strongest

(G) CM p300 bioChIP-seq test characteristics based on the Vista Enhancer Database. CM, E12.5, and E16.5 ventricular CMs. Heart, E12.5 ventricular tissue. FB, E12.5 forebrain.
(H) Heart TF bioChIP-seq signals[15] at CM p300 regions. Average of biological duplicates.
See related Figure S1.

Please cite this article in press as: Zhou et al., Dynamic changes in P300 enhancers and enhancer-promoter contacts control mouse cardiomyocyte maturation, Developmental Cell (2023), https://doi.org/10.1016/j.devcel.2023.03.020

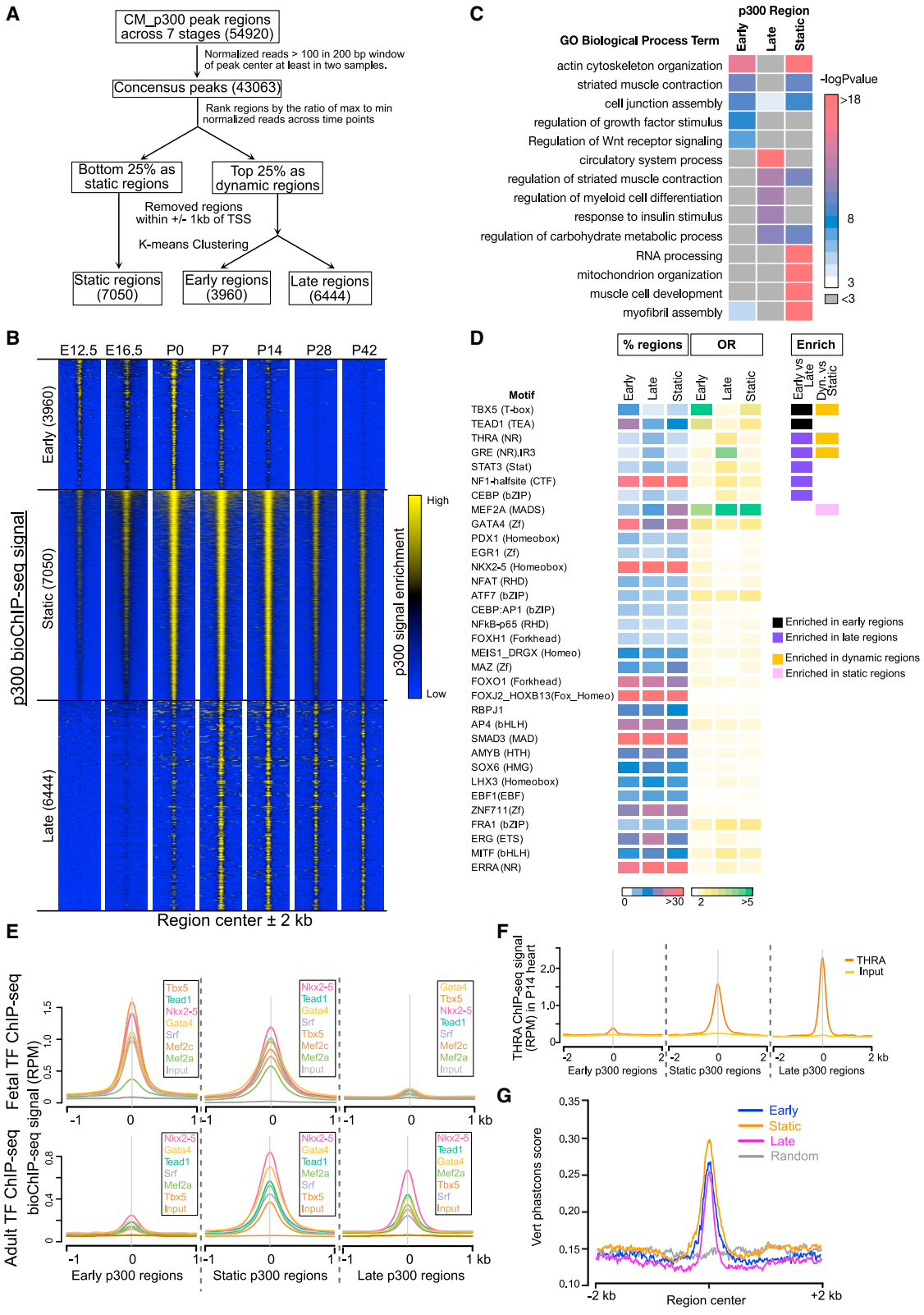

Figure 2. Characterization of P300 dynamic enhancers during heart development

(A) Flowchart for identification of dynamic distal P300 regions.

(B) P300 signal in early, static, and late regions.

(legend continued on next page)

to weakest signal across the time course. The quartiles with the greatest and smallest temporal variation in signals were defined as "dynamic" and "static" P300 regions, respectively (Figure 2A; Data S1). After the exclusion of regions within 1 kb of TSSs, K-means clustering of the dynamic and static regions yielded early (3,960 dynamic regions), late (6,444 dynamic regions), and static (7,050 static regions; Figure 2B) regions. Most GO terms linked to early and late regions did not overlap (Figure 2C). Among these were "regulation of growth factor stimulus" and "regulation of Wnt receptor signaling," associated with early regions; "regulation of myeloid cell differentiation" and "response to insulin stimulus," enriched in late regions; and "RNA processing" and "mitochondrion organization," enriched in static regions.

To identify TFs that recruit P300 in the three region classes, we scanned for TF motif enrichment. Motifs of cardiac TFs TEAD1, GATA4, and MEF2 were enriched in all three classes of P300 regions (Figure 2D). The TBX5 motif was enriched in early but not in late or static regions, consistent with TBX5 downregulation and its reduced binding signal in adult P300 regions (Figure 1H). Among the motifs enriched in the late P300 regions were several nuclear receptors (NRs), such as THRA and the glucocorticoid receptor, which are known to regulate CM maturation *in vivo* and in iPSC-derived CMs.[8,27,28]

Cardiac TF occupancy signals were concordant with P300 occupancy at dynamic and static P300 regions. Early and late P300 regions had strong TF occupancy at the congruent developmental stage. Static regions showed strong TF occupancy at both stages (Figure 2E). Again, TBX5 showed the most dynamic changes between fetal and adult hearts and between early and late P300 regions. We also examined THRA occupancy of these regions using a P15 cardiac THRA occupancy data.[8] THRA occupancy was strongest in late P300 regions and static P300 regions and weak at early P300 regions (Figure 2F).

Evolutionary conservation of enhancers is indicative of biological function that is essential for reproductive fitness. Early, late, and static P300 regions were all strongly conserved (Figure 2G). The aggregate conservation scores were substantially higher than those of the set of heart enhancers marked by H3K27ac and slightly higher than those of heart enhancers bound by multiple cardiac TFs.[15]

High-throughput validation of enhancer activity during *in vivo* murine CM development

To test whether dynamic P300 regions show developmentally regulated enhancer activity, we used adeno-associated virus serotype 9 (AAV9)-based massively parallel reporter assay (MPRA) to measure their *in vivo* activity in CMs. In the heart, AAV9 selectively transduces CMs. We designed an MPRA vector in which a minimal promoter is placed upstream of a mCherry reporter (Figures 3A and S2A). In pilot studies, enhancer reporter AAV containing one of three Early P300 regions located −5, +14, and +20 kb from the *Bmp10* TSS (Figure 1F) was delivered at E15.5 or P0 (Figures 3A and 3B). Poor AAV9 transduction before E15.5 made earlier developmental stages experimentally inaccessible. Ventricular mCherry expression driven by each enhancer was present at P0 and was weaker at P7 and P28 (Figure 3C). Quantitative PCR comparing reporter RNA to DNA confirmed this temporal pattern (Figures 3D and 3E).

Having validated that AAV enhancer reporters capture dynamic enhancer activity in CMs *in vivo*, we performed an AAV-MPRA to determine whether dynamic P300 binding predicts dynamic enhancer activity. Using pooled oligonucleotide synthesis, we generated a library of 400 bp regions centered on 685 early and 1,231 late P300 regions (Figure 3F). This library also contained static regions, regions bound by multiple TFs,[15] P300 regions adjacent to strongly expressed cardiac genes, positive control regions previously validated by AAV-MPRA[15] or transient transgenesis,[18] and negative control regions comprising brain or embryonic stem cell P300 regions, random intergenic regions, and regions without activity in transgenic assays.[18] CM P300 signal was the strongest in positive controls, the weakest in negative controls, and intermediate in the dynamically regulated P300 regions (Figure S2B). The enhancer library was cloned into the mCherry reporter's 3′ untranslated region, so that the enhancer drives its own transcription (Figure 3F) to enable sequencing-based enhancer activity measurement.[29] The pooled AAV library was delivered to E15.5 embryos or newborn mice, and ventricles were collected at P0, P7, and P28, with 12–28 replicates per time point. Although the MPRA assay was performed with variable times between library delivery and enhancer activity measurement, for intervals of 4 days or longer, these changes did not significantly alter activity measurements (Figures S2C–S2F). Amplicons containing the test regions were quantified by sequencing heart RNA and AAV DNAs. Regions with low coverage in the AAV DNA library were excluded (Figure S2G). Correlation between the remaining regions was high across the three time points (Figure S2H).

Regions were ranked by enhancer activity, the ratio of reads from RNA to AAV DNA (Figures 3G and S2I; Data S2). Positive and negative control regions had high and low enhancer activities, respectively (Figures 3G and S2I). The 95th percentile of the negative control regions defined the 5% false discovery threshold. Among the 685 early P300 regions tested, 16% (110) were active at P0; 14% (94), at P7; and 8% (57), at P28. Among the 1,231 late P300 regions, 9% (116), 15% (181), and 18% (220) were active at P0, P7, and P28, respectively. The relatively low frequency of P300 regions with activity in this assay suggests that it is relatively less sensitive than transient transgenesis, potentially due to the smaller size of tested elements and the use of dynamic regions, which tended to have lower P300 signals. We then analyzed the dynamic activity of the subset of regions with the activity in at least one time point. Early P300 regions demonstrated significantly reduced enhancer

(C) Top 5 GO terms enriched among early, static, and late P300 regions.
(D) Enriched TF motifs in P300-bound regions. OR, odds ratio; NR, nuclear receptor.
(E) Cardiac transcription factor (TF) bioChIP-seq signal[15] at P300 peaks. Average of biological duplicates.
(F) THRA ChIP-seq signal in P15 hearts[8] centered at P300 peaks.
(G) Phastcons scores at early, static, and late P300 regions.
See related Figure S1.

Please cite this article in press as: Zhou et al., Dynamic changes in P300 enhancers and enhancer-promoter contacts control mouse cardiomyocyte maturation, Developmental Cell (2023), https://doi.org/10.1016/j.devcel.2023.03.020

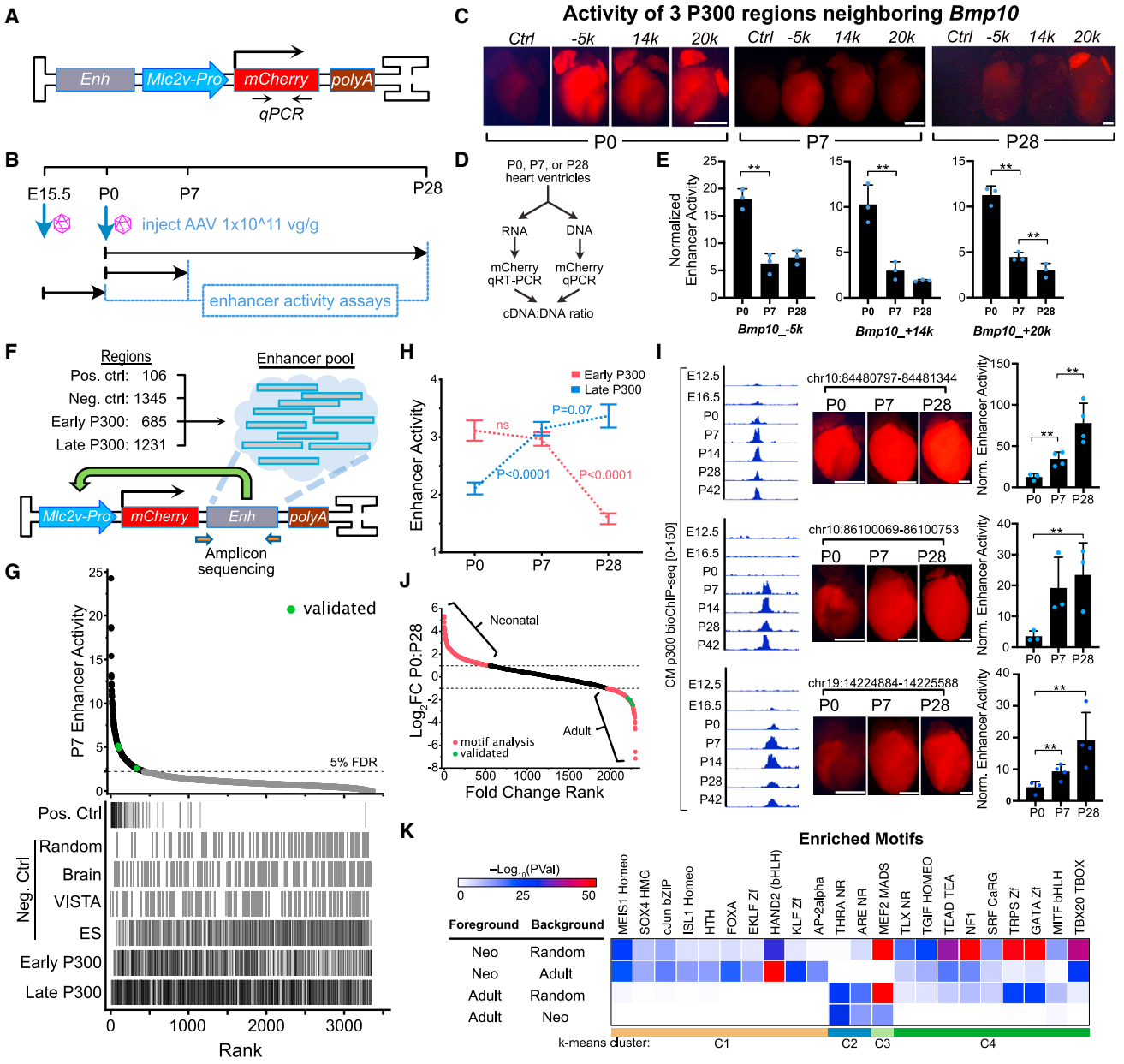

Figure 3. Enhancer activity of dynamic P300 regions during *in vivo* CM development

(A) AAV vector for testing cardiac enhancer activity.

(B) Timeline for MPRA experiments.

(C) Representative images of enhancer activity of three early P300 regions flanking *Bmp10* (see Figure 1F). Scale bars, 1 mm.

(D and E) Quantification of individual enhancer activity. Activities of −5,000, +14,000, and +20,000 *Bmp10* enhancers were normalized to vectors lacking enhancer. t test: **p < 0.01.

(F) Design of MPRA to measure early P300 and late P300 region activities. Synthesized 400 bp regions were cloned into the 3′ UTR of a basal promoter-mCherry AAV reporter.

(G) MPRA results. Lower line plot indicates the annotation assigned to each region.

(H) MPRA activity of early P300 and late P300 regions at P0, P7, and P28. Early P300 group, 685 regions; late P300 group, 1,231 regions. n = 12 biological replicates at P0; n = 28 at P7 and P28. Steel-Dwass. ns, not significant.

(I) Activity of three selected late P300 regions with increasing MPRA activity. Left, P300 bioChIP signal. Middle, representative images. Right, quantification. t test: **p < 0.01. Scale bars, 1 mm.

(J and K) Motifs enriched in regions with selective neonatal or adult MPRA activity. Non-redundant motifs with significant enrichment (Neg. $\log_{10}$ p value > 10) are shown.

See related Figure S2.

Please cite this article in press as: Zhou et al., Dynamic changes in P300 enhancers and enhancer-promoter contacts control mouse cardiomyocyte maturation, Developmental Cell (2023), https://doi.org/10.1016/j.devcel.2023.03.020

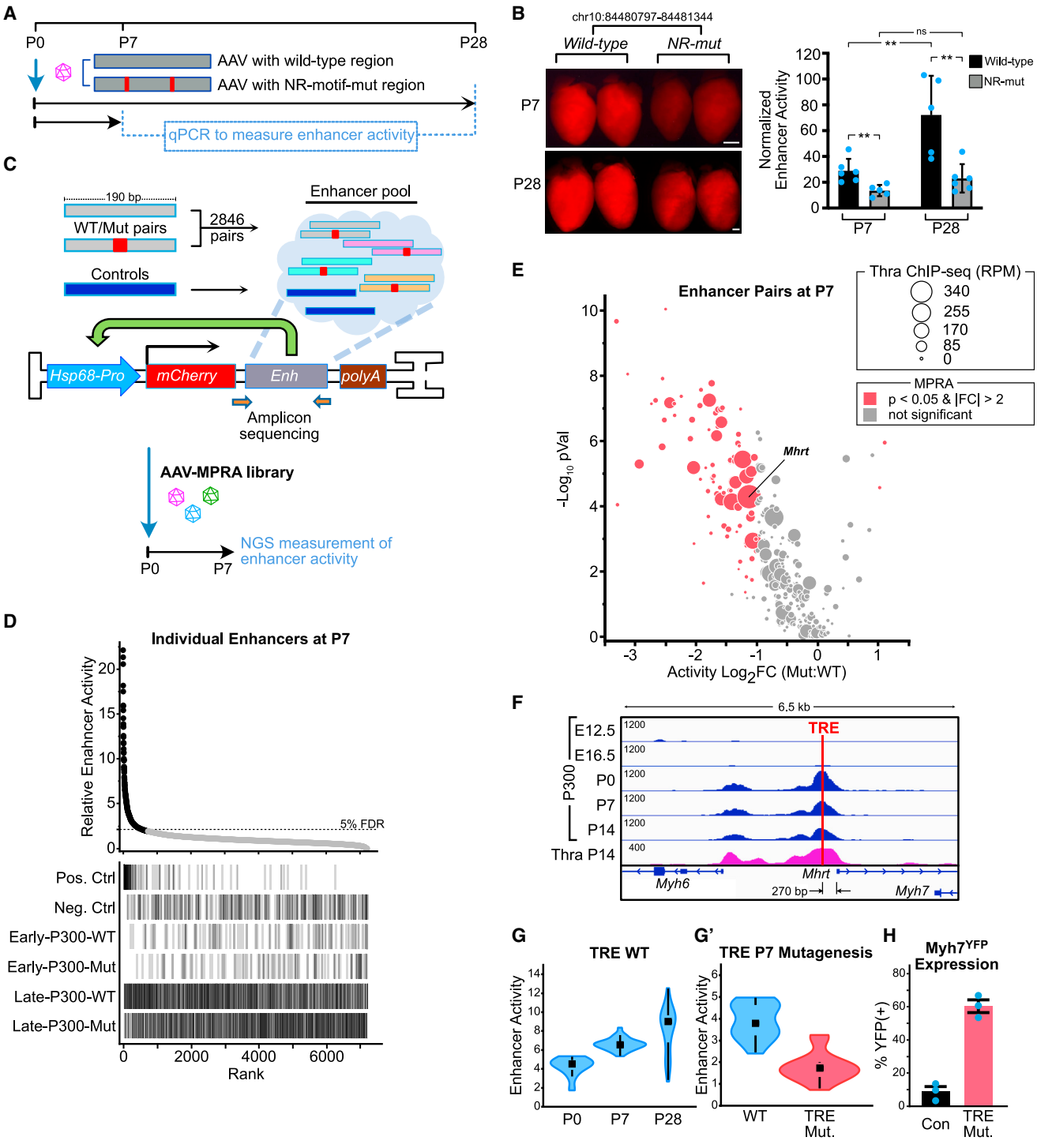

Figure 4. The nuclear receptor motif is essential for activation of late P300 regions

(A) Cardiac enhancer activity of NR motif-containing late P300 regions was measured with or without NR motif mutation.

(B) Representative mCherry reporter images and enhancer activity quantification. Scale bars 1 mm. t test: **p < 0.01.

(C) MPRA to probe the requirement for nuclear receptor (NR) motifs. NR motif-containing P300 regions were synthesized as wild-type and mutant pairs and inserted into the AAV-MPRA vector.

(D) MPRA result measured at P7. RNA/DNA ratio was normalized to the mean value of the negative control group. Activity threshold was set at the negative control 95th percentile. Line plot indicates the annotation assigned to each region.

(E) Effect of NR mutation on 337 WT:Mut pairs with detectable MPRA activity at P7. Paired t test. Marker size indicates thyroid hormone receptor A (THRA) ChIP-seq signal in P15 heart (GSE125414). n = 14 biological replicates.

(legend continued on next page)

Please cite this article in press as: Zhou et al., Dynamic changes in P300 enhancers and enhancer-promoter contacts control mouse cardiomyocyte maturation, Developmental Cell (2023), https://doi.org/10.1016/j.devcel.2023.03.020

activity at P28 compared with that at P0 and P7, and late P300 regions showed significantly elevated enhancer activity at P7 and P28 compared with that at P0 (Figures 3H and S2J). Three late P300 regions with dynamic enhancer activity in the MPRA assay were individually validated *in vivo* using AAV enhancer reporters. Fluorescent imaging and quantitative PCR confirmed that these regions gain enhancer activity between P0 and P28 (Figure 3I).

We performed the motif analysis to define TFs that contribute to the temporal regulation of these experimentally validated dynamic regions. Neonatal and adult regions with the strongest change in enhancer activity ("neonatal" = $\log_2$ fold-change < -1 [n = 554]; "adult" = $\log_2$ fold-change > 1 [n = 347]; Figure 3J) were strongly enriched for MEF2, GATA, and TEAD motifs when compared with random backgrounds (Figure 3K). To highlight motifs with strong differential enrichment between neonatal and adult MPRA regions, we compared the neonatal foreground with the adult background and vice versa. This demonstrated the strong enrichment of TBX (T-box) and HAND (bHLH) motifs in neonatal regions, and NR motifs of THRA and estrogen related receptor alpha (ESRRA) in adult regions (Figure 3K). These data are consistent with the important roles of T-box and HAND factors in heart development[30] and THRA[27] and estrogen-related receptor[31] for CM maturation.

NR motifs are required for postnatal CM enhancer activation

To assess the contribution of NR motifs to the activity of late P300 regions, we mutated an NR binding motif in one of the individually validated late P300 regions (Figure 3I). The NR motif mutation prevented developmental enhancer activation, resulting in an activity decrease of 50% at P7 and 70% at P28 (Figures 4A and 4B).

To more systematically validate the importance of the NR motif in late P300 region activation, we generated an AAV-MPRA library containing WT-Mut pairs of 120 early regions, 2,705 late P300 regions, and a subset of positive and negative control regions (Figure 4C). Pooled AAV library was administered at P0 and analyzed at P7 by amplicon sequencing. We excluded regions with low coverage in AAV library DNA (Figure S3A) and then calculated enhancer activity by the ratio of read counts in RNA vs. DNA amplicons. Replicates correlated well (Figure S3B). Of the 2,825 tested dynamic regions, 11.9% (337) had detectable activity in a member of the WT-Mut pair (activity greater than 95% of the negative controls; Figure 4D; Data S3). This low activity frequency likely reflects the small size (190 bp) of tested regions and their centering on the NR motif. Of the pairs with detectable activity, enhancer activity significantly differed between WT and Mut in 86 pairs (paired t test adj. $p < 0.05$ and absolute fold-change > 2; Figure 4E; Data S3). Notably, 97.7% of these were downregulated by the NR motif mutation, indicating that in most cases, these NR motifs promote enhancer activation.

THRA is an NR that is a well-established regulator of CM maturation, including the perinatal switch of myosin from *Myh7* to *Myh6*.[8] Overlaying P15 heart THRA occupancy[8] and NR mutagenesis MPRA datasets demonstrated that many of the essential NR motifs are bound by THRA *in vivo* (Figure 4E). At the *Myh6/Myh7* locus, a late P300 enhancer containing a THRA-bound thyroid hormone response element (TRE) falls in the intergenic region, close the promoter for *Mhrt*, a long non-coding RNA antisense to *Myh7* that contributes to *Myh7* repression in adult CMs.[32] The MPRA data demonstrated that postnatal activation of this enhancer required the TRE (Figure 4G). Using Cas9- and AAV-mediated somatic mutagenesis,[33] we ablated the TRE in the native locus at birth. TRE mutagenesis, largely confined to the TRE motif (Figure S3C), resulted in persistent *Myh7* expressions, as reported by yellow fluorescent protein (YFP) fluorescence from a $Myh7^{YFP}$ knockin allele (Figures 4H and S3D).

Dynamic P300 enhancers are linked to developmental changes in 3D genome architectures

The contribution of 3D chromatin structures to gene regulation during later stages of development has been little studied. We performed Hi-C[34] on E12.5, P0, and P42 murine ventricular CMs (Figure 5A). For each of the three replicates for each stage, we obtained more than 500 M reads, allowing intra-chromosomal (*cis*) interactions to be assessed with 5 kb resolutions (Figure S4A). The biological replicates were highly reproducible, and intragroup variation was much smaller than the variation between time points (Figure S4B). The reads from each time point were pooled for subsequent analyses. A representative contact map illustrates two developmentally regulated chromatin loops that connect the *Synpo2* TSS to dynamic P300 regions within an adjacent gene (Figure 5B).

We detected 7,991, 8,332, and 9,747 notable loops at E12.5, P0, and P42, respectively (Figure S4C; Data S4), a comparable number with an independent study of adult mouse CMs.[35] However, 40% of the loops were shared between all-time points, whereas 20% and 40% were found in two or only one time point, respectively (Figure S4D). Loops were overrepresented for P300 regions (hypergeometric test: $p < 1.4E{-}196$). Late P300 regions had a stronger loop to promoters in adults compared with fetal CMs (Figure 5C). However, contact scores of early P300 region loops to promoters did not significantly differ between stages, despite their difference in P300 occupancy (Figure 5C).

Based on Hi-C data, the genome can be categorized into active (A) and repressive (B) compartments.[34] In addition, 90.2% of the genome remained in the same compartment at both stages, and 4.3% switched from A to B ("A → B chromatin") and 5.5% from B to A ("B → A chromatin"; Figures 5D and S5A; Data S5). Consistent with P300 marking active enhancers, A → B chromatin had 3.1-fold more early than late P300 regions and the greatest early P300 region density (Figures 5E and S5B). By contrast, B → A chromatin had

(F–H) Activity of late P300 region near *Mhrt* promoter requires thyroid response element (TRE). (F) THRA- and P300-bound TRE within the *Myh6/Myh7* locus. (G) P300 enhancer activity, from Figure 3 MPRA. n = 12. (G′) Enhancer inhibition by TRE mutation, from (D) MPRA. n = 14. (H) Myh7 silencing, measured by YFP FACS in P28 $Myh7^{YFP}$ CMs with or without somatic mutagenesis of endogenous TRE.
See related Figure S3.

Please cite this article in press as: Zhou et al., Dynamic changes in P300 enhancers and enhancer-promoter contacts control mouse cardiomyocyte maturation, Developmental Cell (2023), https://doi.org/10.1016/j.devcel.2023.03.020

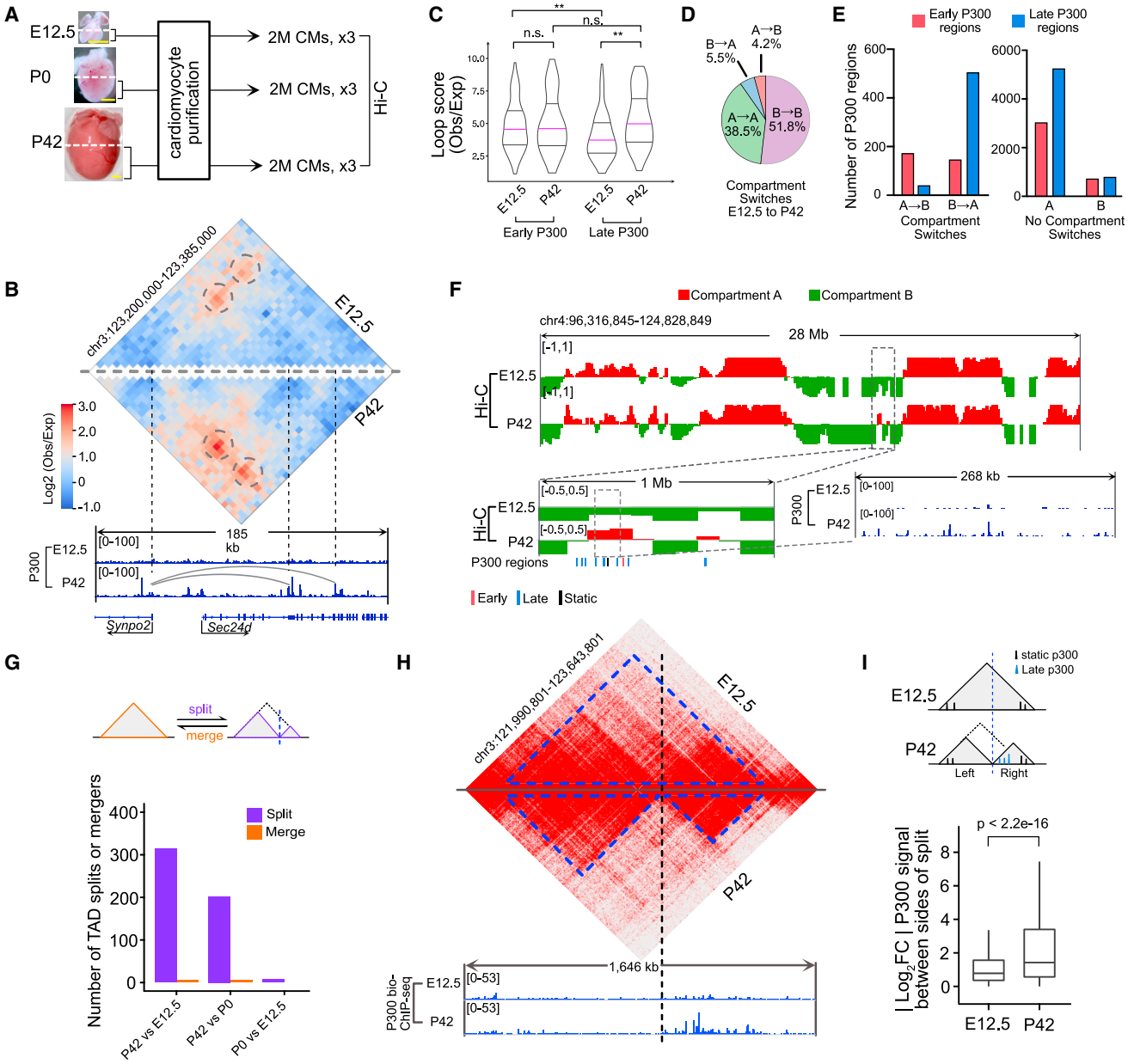

Figure 5. Correlation of dynamic P300 binding to chromatin conformation

(A) CM samples used to generate HiC data. Scale bars, 1 mm.

(B) Representative Hi-C contact map and the corresponding P300 bioChIP-seq tracks.

(C) Interaction score of loops between early (n = 104) or late (n = 141) P300 regions and TSS. Wilcoxon ranked sum test.

(D) Percentage of genome in compartments that were stable (90.2%), A → B (4.3%), or B → A (5.5%), between E12.5 and P42.

(E) Distribution of P300 regions in stable and switching compartments.

(F) Representative region (dashed box, enlarged in tracks below) that underwent B → A switch and the corresponding CM P300 bioChIP-seq tracks.

(G) Total number of TAD splits or mergers between E12.5, P0, and P42.

(H) Representative example of a TAD split and P300 bioChIP signal in daughter TADs.

(I) P300 signal between daughters of split TADs at E12.5 (pre-split) and P42 (post-split). n = 314.

See also related Figures S4 and S5.

2.4-fold more late than early P300 regions and the highest late P300 region density (Figures 5E and S5B). B → A chromatin switching occurred both by spreading at the edge of a pre-existing A domain (Figure S5C) and by generating A domains *de novo* inside of B domains (Figure 5F). Late P300 regions were enriched in both types of B → A switching. P300 deposits H3K27ac, which modulates chromatin folding.[36] Thus, the correlation between dynamic P300 occupancy and chromatin compartment transitions suggests that P300 binding is a driving force behind chromatin domain switching during CM maturation.

Please cite this article in press as: Zhou et al., Dynamic changes in P300 enhancers and enhancer-promoter contacts control mouse cardiomyocyte maturation, Developmental Cell (2023), https://doi.org/10.1016/j.devcel.2023.03.020

Hi-C data can also be used to identify self-interacting chromatin regions named topologically associating domains (TADs). TADs can "split" or "merge" through the strengthening or weakening of the boundaries. We used our TADsplimer algorithm[37] to detect TAD splits and mergers between time points. We detected about 7,000 TADs at each time point (Figure S5D). Consistent with previous studies,[37] only ~4% of the TADs split or merged between developmental stages. Most were TAD splits, and most occurred during postnatal CM maturation (Figures 5G and S5E). A representative TAD split demonstrated a predominance of late P300 regions on one side of the split TAD (Figure 5H). To evaluate whether this is a common feature of split TADs, we compared the ratio of the P300 signal on each side of the split TAD at E12.5 (pre-split) and P42 (post-split). There was a greater difference between P300 signals on each side of the TAD post-split than pre-split (Figure 5I). These data suggest that the developmental enforcement of TAD boundaries restricts the spatial domain of P300 activation.

3D genome-mediated regulation of CM developmental gene expression

We profiled the developmental changes in CM gene expressions by sequencing bulk RNA isolated from purified CMs in biological triplicates at the same seven stages from E12.5 to P42 (Figure S6A; Data S5). Principal component analysis (PCA) showed the clustering of replicates from each time point and the separation of time points along the first principal component (Figure S6B). We identified differentially expressed genes (DEGs) between fetal and adult stages (average of P28 and P42 compared with an average of E12.5 and E16.5: $p_{adj} < 0.01$ and absolute $\log_2FC \geq 3$; Figure 6A). Genes with known developmental regulation showed the expected temporal patterns (Figure S6C), supporting the RNA-seq data quality. This was further confirmed by the GO analysis: the 493 adult DEGs were associated with fatty acid metabolism, ion transport, and cellular response to hormone stimulus (Figure 6B), and the 783 fetal DEGs were related to cell cycle, heart development, and DNA packaging (Figure 6B), consistent with well-established changes during CM maturation.[5]

We analyzed the effect of 3D genome changes on developmentally regulated CM gene expressions. Genes within A → B chromatin and B → A chromatin were downregulated and upregulated, respectively, between E12.5 and P42 (Figure 6C). Moreover, the developmental splitting of TADs, which increased the difference in mean P300 signal between the left and right daughter TADs (Figure 5I), was mirrored by an increased difference in the mean gene expression between daughter TADs (Figure 6D). A representative example demonstrates gain in the P300 signal on the right side of a TAD split (blue dotted line; Figure 6E). Several genes selectively expressed in mature CMs, including *Myoz2* and *Synpo2*, are upregulated in this right-sided daughter TAD. Adult DEGs contained within split TADs were enriched for GO terms including metabolic process, heart development, and regulation of heart rate, whereas fetal DEGs within split TADs were enriched for the terms including cell cycle and cell division (Figure S6D), suggesting that TAD splitting promotes CM maturation.

Enhancer regulation of a target gene is a function of enhancer strength and contact frequency between the enhancer and the gene's promoter. The "activity-by-contact" (ABC) model implements this concept as a score based on the product of enhancer strength (A) and enhancer-promoter (E-P) contact strength (C), summed across the enhancers linked to each gene.[38] We calculated the ABC scores using stage-specific P300 signals and Hi-C contact scores. As expected, the ABC scores of fetal DEGs were higher in fetal CMs, and the scores of adult DEGs were higher in adult CMs (Figure 6F). We used the ABC score to investigate the contribution of P300 signals and chromatin looping to developmental gene expression genome-wide. Developmental changes in ABC scores and gene expressions significantly correlated ($r = 0.59$, $p = 1.1E{-}258$, Figure 6Gi). By contrast, ABC scores calculated using stage-matched P300 signals and stage-mismatched Hi-C contact scores only correlated weakly with gene expression changes ($r = 0.20$, Figure 6Giv). This analysis highlights the importance of developmental changes in 3D genome organizations, in combination with the developmental regulation of enhancers, to maturational changes in gene expressions.

We used the Hi-C contact matrices to analyze the relationship between promoter-distal region contact frequency and genomic distance genome-wide. This relationship changed between E12.5 and P42 so that adult promoters tended to contact regions that were closer along the primary DNA sequence (Figure 6H). Consistent with this result, adult DEGs were closer to the nearest P300 region than fetal DEGs (Figure S6E). We evaluated whether this aggregate contact vs. distance relationship could substitute for the actual Hi-C contact frequencies in the ABC model. The aggregate contact frequency vs. the distance relationship performed nearly as well ($r = 0.52$, Figure 6Gii) as the actual contact data ($r = 0.59$, Figure 6Gi). However, calculating the aggregate contact frequency using the stage-mismatched contact frequency-distance relationship resulted in a much lower correlation ($r = 0.34$, Figure 6Jiii), suggesting that the developmental change in the contact frequency-distance relationship is functionally important.

Hi-C provides a global view of the 3D genome but has relatively low sensitivity—the number of called loops (~8,700 per time point) greatly underestimates actual chromatin contacts. Therefore, we performed H3K27ac HiChIP[39] on purified E12.5 and P42 ventricular CMs (Figures 7A and S7A). Replicates correlated well (Figure S7B). We identified 68,464 fetal and 74,530 adult reproducible loops (>5 reads in each sample; Data S6). These were categorized as enhancer-enhancer (E-E, 59%), E-P (33%), and promoter-promoter (P-P, 8%) (Figure 7B). However, 27,605 (40.3%) and 33,671 (45.2%) loops were called only at E12.5 or P42, respectively, whereas 40,859 were shared by both stages (Figure 7B). Quantitative analyses likewise showed that many loops (19.5%) had significantly different contact scores at E12.5 and P42 ($p_{adj} < 0.05$ and $|\log_2FC| > 2$; Figure 7C). Genome browser views of *Bmp10* and *Myh6/Myh7* loci, shown in Figures S7C and S7D, illustrate developmentally regulated loops and P300 occupancy. E12.5-selective and P42-selective loops were enriched for early and late P300 regions, respectively (Figures 7D and S7E). Genes linked to early and late P300 regions by strong HiChIP loops were more highly expressed at E12.5 and P42, respectively (Figure 7E). Conversely, P300 regions with HiChIP loops to fetal or adult DEGs had greater P300 signals at E12.5 and P42, respectively (Figure S7F).

Please cite this article in press as: Zhou et al., Dynamic changes in P300 enhancers and enhancer-promoter contacts control mouse cardiomyocyte maturation, Developmental Cell (2023), https://doi.org/10.1016/j.devcel.2023.03.020

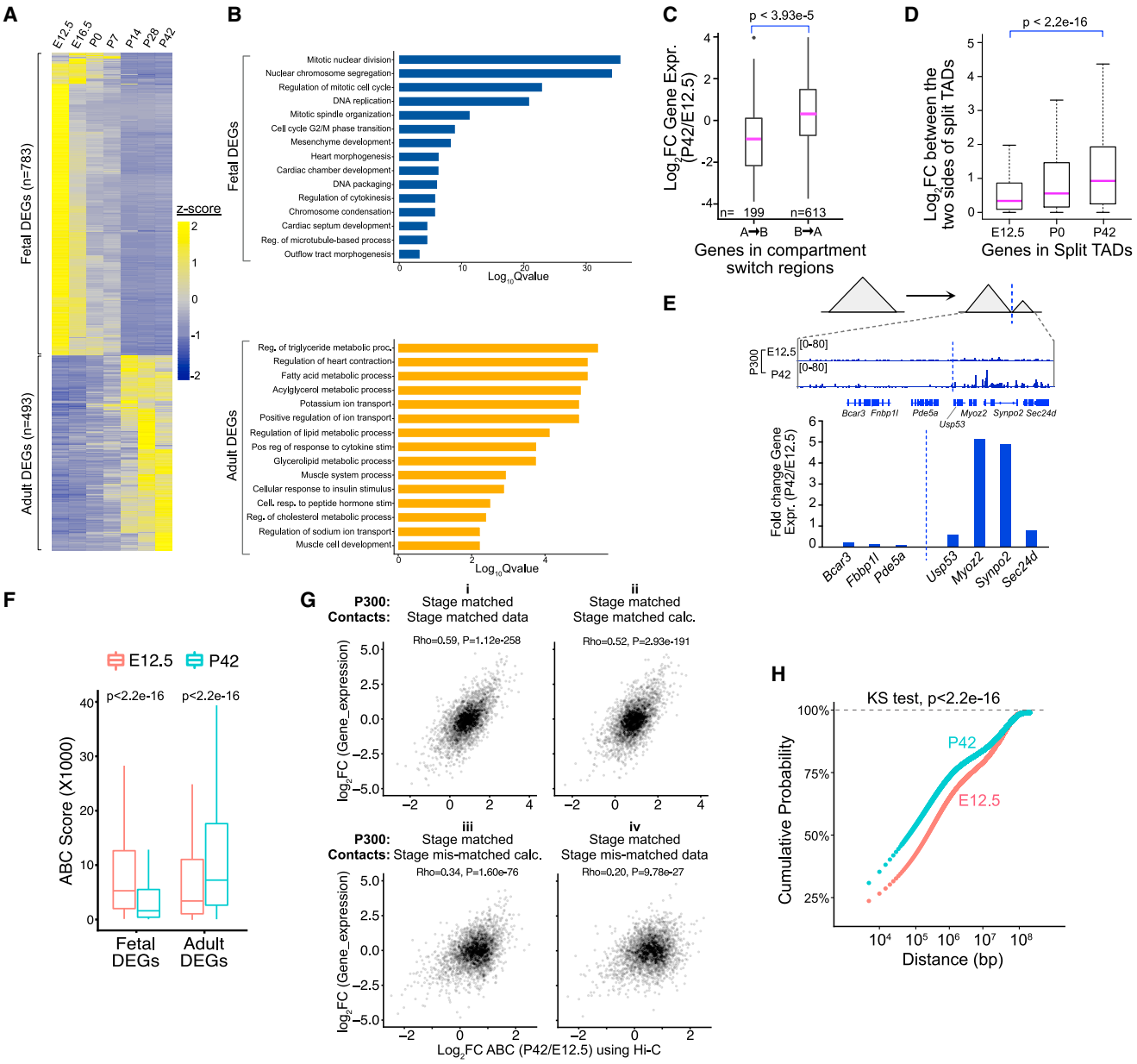

Figure 6. Interaction between developmental changes in P300 occupancy and 3D chromatin structure modulate CM gene expressions

(A) Differentially expressed genes (DEGs; $p_{adj} < 0.01$ and absolute $log_2FC \geq 3$) in CMs from E12.5 to P42. Hierarchical clustering.

(B) Gene ontology terms enriched among fetal and adult DEGs.

(C) Expression of genes in chromatin that underwent A and B switches between E12.5 and P42.

(D) Expression of genes in left and right sides of split TADs at E12.5, P0, and P42. Wilcoxon ranked sum test. n = 314.

(E) Representative example of TAD splitting and gene expression changes.

(F) ABC scores of fetal (n = 235) and adult (n = 265) DEGs with EP loops at E12.5 and P42. Wilcoxon ranked sum test.

(G) Correlation between developmental change in gene expression and change in ABC scores. Gene expression values from E12.5 and P42. Contact scores were from (Gi) Hi-C data, (Gii) genome-wide distance-contact score relationships at E12.5 and P42 (see H), (Giii) stage-swapped distance-contact score relationships, and (Giv) stage-swapped Hi-C data.

(H) Cumulative distribution function of the genome-wide average frequency of contacts between a region and the TSS as a function of their genomic distance. Kolmogorov-Smirnov (KS) test.

Related to Figure S6.

Typical enhancers cluster into regulatory centers termed super-enhancers (SEs).[40] Using P300 occupancy data, we identified 1,319 SEs at E12.5 and P42. However, 150 and 472 were unique to E12.5 or P42, respectively, (Figure 7F; Data S7) and were enriched for early or late P300 regions, respectively (Figure 7G). SE chromatin contact density, calculated from HiChIP,

Please cite this article in press as: Zhou et al., Dynamic changes in P300 enhancers and enhancer-promoter contacts control mouse cardiomyocyte maturation, Developmental Cell (2023), https://doi.org/10.1016/j.devcel.2023.03.020

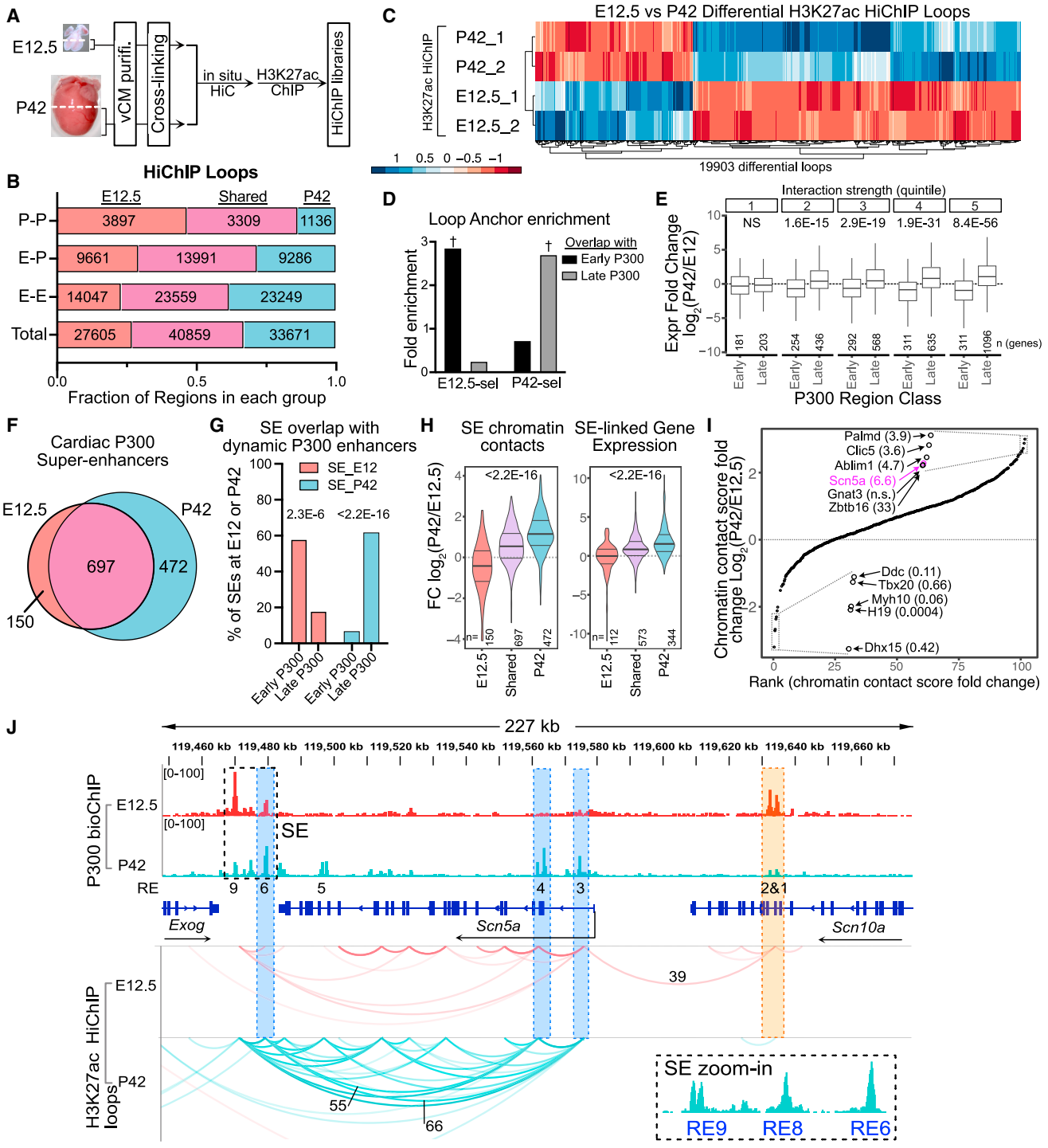

Figure 7. Interaction between developmental changes in P300 occupancy, 3D chromatin structure, and gene expression

(A) H3K27ac Hi-ChIP workflow. vCMs, purified ventricular CMs.

(B) H3K27ac Hi-ChIP loops called at E12.5 and P42. E-E, enhancer-enhancer; E-P, enhancer-promoter; P-P, promoter-promoter.

(C) Differential loops (p_{adj} < 0.05 and absolute log_2FC > 2) between E12.5 and P42.

(D) Enrichment of P300 early or late enhancers at E12.5- or P42-selective loop anchors, compared with all other loops. †Fisher p < 2.2E−16.

(E) Developmental change in expression of genes linked to early or late P300 enhancers by E-P loops, categorized by quintile of HiChIP loop strength at E12.5 (early P300) or P42 (late P300). Wilcoxon ranked sum test with Holm's multiple testing correction.

(F) CM super-enhancers (SEs) identified at E12.5 and P42 by P300 bioChIP-seq signal.

(G) Enrichment of early or late P300 regions in E12.5 or P42 SEs. Proportions test.

(H) Ratio of SE chromatin contacts (left) or expression of genes (right) linked to SEs by HiChIP loops at E12.5 and P42. Kruskal-Wallis test.

(legend continued on next page)

was also developmentally regulated, with E12.5-selective and P42-selective SEs having greater interactions at the congruent stage (Figure 7H). Indeed, developmental changes in SE P300 signals, SE chromatin contact densities, and expressions of genes linked to these SEs by chromatin contacts correlated with one another (Figures 7H and S7G).

To examine the contribution of SE interaction changes to developmentally regulated gene expressions, we focused on SEs shared between E12.5 and P42, which by definition have fewer developmental changes in P300 signals. A subset of Shared SEs exhibited large changes in contact densities between the stages (Figure 7I). Those with the greatest changes in contact densities were associated with corresponding developmental changes in gene expressions, suggesting that the changes in SE interactions and strength contribute to target gene regulation. A notable example is a previously characterized SE linked to *Scn5a*,[41,42] encoding the cardiac sodium channel. The *Scn5a* locus contains several previously characterized regulatory elements (REs). RE6–9 comprise the SE, which is present at E12.5 and P42 (Figure 7J). RE1–2 and RE3, 4, and 6 have developmentally downregulated and upregulated P300 occupancy, respectively. Correspondingly, RE1–2 lost contact with the *Scn5a* TSS, whereas contacts between RE3–9, including RE6–9 within the SE, increased with each other and the *Scn5a* TSS in mature CMs (Figure 7J). Thus, the 6.6-fold upregulation of *Scn5a* between E12.5 and P42 is associated with marked increases in SE-promoter contacts.

These results suggest that the interaction of developmental changes in P300 occupancy and 3D chromatin structures contributes to developmentally regulated CM gene expression.

DISCUSSION

We generated a rich data resource for the integrative investigation of CM-specific P300 binding, enhancer activity, *cis*-regulatory motifs, 3D genome, and transcriptome at multiple time points during *in vivo* CM differentiation and maturation.

A fundamental question in development is how stage-specific enhancers are established and maintained. Our dataset of P300 enhancers across seven developmental stages from fetal-to-adult CMs suggests that the differential binding of TFs mediates the differential P300 binding to different genomic loci during CM development and maturation. TF ChIP-seq and motif enrichment in fetal P300 regions and P300 regions with neonatal MPRA activity most strongly implicated TBX5, TEAD, and HAND in the early recruitment of P300. At later developmental stages, these analyses implicated the NR and MEF2 motifs. There has been growing appreciation of the importance of NRs, including THRA, estrogen-related receptors, and PPARGC1A in CM maturation.[8,9,31,43,44] These NRs bind P300, sometimes in a ternary complex with MEF2.[45–47] We used AAV-MPRA to validate the key functions of NRs and NR motifs in promoting P300 binding and the activation of late P300 regions and to experimentally identify 84 dynamic enhancers that required the NR motif for activity. Many of these validated enhancers were bound by THRA, consistent with its important role in CM maturation.[8] However, other MPRA-validated NR motifs, including many with the strongest effect and nearly all that inhibited enhancer activity, were not bound by THRA at P15, suggesting that these effects are mediated by other NRs.

Current evidence points to causal links between enhancer activation and 3D genome structures. These operate in both directions and are context-dependent. For example, genomic rearrangements that disrupt TADs result in ectopic E-P interactions and gene dysregulation.[48] At the same time, TFs mediated the reorganization of chromatin loops and chromatin compartments during cell differentiation.[49,50] P300 and histone acetylation may mediate some of these effects of TF binding since histone acetylation modulated chromatin loops and compartmentalization and ectopic H3K27ac facilitated the formation of *de novo* loops in leukemia cells.[36] Our data indicate that developmentally regulated binding of TFs and P300 at early and late P300 regions modulate chromatin loops, TADs, compartments, and SEs. Reciprocally, the changes in chromatin conformation mediated by other factors may influence TF and P300 binding and enhancer activity. Determining the mechanisms by which these different levels of regulation affect each other is an important area for future study.

The contribution of 3D genome organizations to the differentiation and maturation of cell lineages has been little studied. We considered three types of 3D genome organizations: loops, TADs, and compartments, which differ in scale and underlying structural mechanisms. CM differentiation between E12.5 and adulthood affected ~20% of HiChIP loops, ~4% of TADs, and ~10% of compartments. Developmentally regulated P300 occupancy interacted with all three types of 3D genome organizations to influence developmental gene expressions in CMs *in vivo*. At the level of the loops, both P300 occupancy signals and contact frequencies influenced developmental gene expressions. Modeling this with the ABC score demonstrated the importance of stage-specific contact frequencies for optimal correlation with developmental gene expressions. This was also seen in SEs, where developmentally regulated contacts of a subset of SEs appeared to play a predominant role in target gene regulation.

TADs have been considered to be conserved between different cell types.[51] We observed that most TADs were constant between fetal and adult CMs. However, we found that a subset of TADs changed during CM development by altered enforcement of TAD boundaries. Intriguingly, TAD splits greatly outnumbered mergers during CM differentiation. This progressive enforcement of within-TAD boundaries during CM maturation confined the domains of chromatin activation and may be a mechanism to constrain gene expressions within highly specialized cell types. It will be interesting to determine whether this mechanism is deployed in other cell types.

We discovered a surprising global developmental shift in the relationship between genomic distance and promoter-distal region contact frequencies; hence, the promoter-distal region

(I) Variation in chromatin contact scores at E12.5 vs. P42 for SEs shared between E12.5 and P42. Boxed regions are magnified and labeled with SE-associated genes and their expression fold-change (P42/E12.5). *Scn5a* (magenta) is shown in (J).
(J) SE at the *Scn5a* locus. Average loop scores for selected loops are labeled. Loops with scores <15 are omitted for clarity.
Related to Figure S7.

distance tends to be shorter in adult CMs. This correlates with the closer average location of the TF binding sites to promoters in adult compared with fetal CMs.[15] This shift is likely functionally important because the contact values calculated from the stage-matched relationship yielded ABC scores that correlated nearly as well with the developmental changes in gene expressions as the actual contact data, whereas values calculated from the stage-mismatched relationship yielded poorly correlating ABC scores. Whether similar shifts in this relationship will be observed in other maturing cell types and the underlying mechanisms will be interesting questions for further study.

Limitations of the study

Our study had limitations. Mice from both genders were pooled. The MPRA enhancer activity measurements were made in episomes and may differ from regulation at the endogenous locus. Inefficient AAV9 transduction before E15.5 precluded enhancer activity early in development by MPRA. MPRA assays measure enhancer activity in limited time points and contexts so that negative activity measurements do not exclude enhancer activity at other time points or contexts. Although Hi-C and H3K27ac HiChIP are state-of-the-art methods to measure 3D genome contacts, they have limited sensitivity and resolution.

STAR★METHODS

Detailed methods are provided in the online version of this paper and include the following:

- KEY RESOURCES TABLE
- RESOURCE AVAILABILITY
  - Lead contact
  - Materials availability
  - Data and code availability
- EXPERIMENTAL MODEL AND SUBJECT DETAILS
  - Mice
- METHOD DETAILS
  - Cardiomyocyte isolation and purification
  - P300 pulldown for Western Blot
  - Immunostaining
  - P300 bioChIP-seq of cardiomyocytes
  - AAV reporter assays
  - Massively parallel reporter assay (MPRA)
  - Amplicon-sequencing of somatic mutagenesis target site
  - Hi-C with mouse cardiomyocytes
  - H3K27ac HiChIP of mouse cardiomyocytes
  - Cardiomyocyte RNA-Seq
  - ChIP-seq data analysis
  - Characterization of P300 enhancer regions
  - RNA-seq data analysis
  - Hi-C data analysis
  - H3K27ac HiChIP data analysis
  - ABC score
  - Super-enhancers
  - Visualization of data with genome browser
- QUANTIFICATION AND STATISTICAL ANALYSIS
  - Statistics

SUPPLEMENTAL INFORMATION

Supplemental information can be found online at https://doi.org/10.1016/j.devcel.2023.03.020.

ACKNOWLEDGMENTS

This study was funded by grants from the National Institutes of Health (P.Z.: U01HL131003; N.J.V.: T32HL007572, F32HL13423501, and K99HL14319; W.T.P.: UM1 HL098166 and R01 HL146634; K.C.: R01GM125632 and R01HL148338).

AUTHOR CONTRIBUTIONS

P.Z. and N.J.V. conceived of the project, designed and performed experiments, analyzed data, and wrote the manuscript. Y.Z. performed bioinformatic analysis and co-wrote the manuscript. Y.C. contributed H3K27ac HiChIP data. R.H. and B.L. contributed Hi-C data. I.S., S.Z., G.W., X.Z., and G.-C.Y. contributed to bioinformatic analysis. Q.M. performed fetal AAV injections. N.M., L.Y., J.C., Y.G., J.Y.L., and W.G. performed experiments. B.R., K.C., and W.T.P. oversaw the project, analyzed data, and co-wrote the manuscript.

DECLARATION OF INTERESTS

The authors declare no competing interests.

Received: February 22, 2022
Revised: February 16, 2023
Accepted: March 5, 2023
Published: April 17, 2023

REFERENCES

1. Schoenfelder, S., and Fraser, P. (2019). Long-range enhancer–promoter contacts in gene expression control. Nat. Rev. Genet. *20*, 437–455.
2. Stadhouders, R., Filion, G.J., and Graf, T. (2019). Transcription factors and 3D genome conformation in cell-fate decisions. Nature *569*, 345–354.
3. Glaser, J., and Mundlos, S. (2022). 3D or Not 3D: Shaping the Genome during Development. Cold Spring Harb. Perspect. Biol. *14*, a040188. https://doi.org/10.1101/cshperspect.a040188.
4. Zheng, H., and Xie, W. (2019). The role of 3D genome organization in development and cell differentiation. Nat. Rev. Mol. Cell Biol. *20*, 535–550.
5. Guo, Y., and Pu, W.T. (2020). Cardiomyocyte maturation: new phase in development. Circ. Res. *126*, 1086–1106.
6. Guo, Y., Jardin, B.D., Zhou, P., Sethi, I., Akerberg, B.N., Toepfer, C.N., Ai, Y., Li, Y., Ma, Q., Guatimosim, S., et al. (2018). Hierarchical and stage-specific regulation of murine cardiomyocyte maturation by serum response factor. Nat. Commun. *9*, 3837.
7. Guo, Y., Cao, Y., Jardin, B.D., Sethi, I., Ma, Q., Moghadaszadeh, B., Troiano, E.C., Mazumdar, N., Trembley, M.A., Small, E.M., et al. (2021). Sarcomeres regulate murine cardiomyocyte maturation through MRTF-SRF signaling. Proc. Natl. Acad. Sci. USA *118*, e2008861118. https://doi.org/10.1073/pnas.2008861118.
8. Hirose, K., Payumo, A.Y., Cutie, S., Hoang, A., Zhang, H., Guyot, R., Lunn, D., Bigley, R.B., Yu, H., Wang, J., et al. (2019). Evidence for hormonal control of heart regenerative capacity during endothermy acquisition. Science *364*, 184–188.
9. Murphy, S.A., Miyamoto, M., Kervadec, A., Kannan, S., Tampakakis, E., Kambhampati, S., Lin, B.L., Paek, S., Andersen, P., Lee, D.-I., et al. (2021). PGC1/PPAR drive cardiomyocyte maturation at single cell level via YAP1 and SF3B2. Nat. Commun. *12*, 1648.
10. Zhang, Y., Li, T., Preissl, S., Amaral, M.L., Grinstein, J.D., Farah, E.N., Destici, E., Qiu, Y., Hu, R., Lee, A.Y., et al. (2019). Transcriptionally active HERV-H retrotransposons demarcate topologically associating domains in human pluripotent stem cells. Nat. Genet. *51*, 1380–1388.

11. Bertero, A., Fields, P.A., Ramani, V., Bonora, G., Yardimci, G.G., Reinecke, H., Pabon, L., Noble, W.S., Shendure, J., and Murry, C.E. (2019). Dynamics of genome reorganization during human cardiogenesis reveal an RBM20-dependent splicing factory. Nat. Commun. *10*, 1538.

12. Kannan, S., Farid, M., Lin, B.L., Miyamoto, M., and Kwon, C. (2021). Transcriptomic entropy benchmarks stem cell-derived cardiomyocyte maturation against endogenous tissue at single cell level. PLoS Comput. Biol. *17*, e1009305.

13. DeLaughter, D.M., Bick, A.G., Wakimoto, H., McKean, D., Gorham, J.M., Kathiriya, I.S., Hinson, J.T., Homsy, J., Gray, J., Pu, W., et al. (2016). Single-cell resolution of temporal gene expression during heart development. Dev. Cell *39*, 480–490.

14. Pinto, A.R., Ilinykh, A., Ivey, M.J., Kuwabara, J.T., D'antoni, M.L., Debuque, R., Chandran, A., Wang, L., Arora, K., Rosenthal, N.A., et al. (2016). Revisiting cardiac cellular composition. Circ. Res. *118*, 400–409.

15. Akerberg, B.N., Gu, F., VanDusen, N.J., Zhang, X., Dong, R., Li, K., Zhang, B., Zhou, B., Sethi, I., Ma, Q., et al. (2019). A reference map of murine cardiac transcription factor chromatin occupancy identifies dynamic and conserved enhancers. Nat. Commun. *10*, 4907.

16. Nord, A.S., Blow, M.J., Attanasio, C., Akiyama, J.A., Holt, A., Hosseini, R., Phouanenavong, S., Plajzer-Frick, I., Shoukry, M., Afzal, V., et al. (2013). Rapid and pervasive changes in genome-wide enhancer usage during mammalian development. Cell *155*, 1521–1531.

17. Visel, A., Blow, M.J., Li, Z., Zhang, T., Akiyama, J.A., Holt, A., Plajzer-Frick, I., Shoukry, M., Wright, C., Chen, F., et al. (2009). ChIP-seq accurately predicts tissue-specific activity of enhancers. Nature *457*, 854–858.

18. Visel, A., Minovitsky, S., Dubchak, I., and Pennacchio, L.A. (2007). VISTA Enhancer Browser–a database of tissue-specific human enhancers. Nucleic Acids Res. *35*, D88–D92.

19. Zhou, P., Gu, F., Zhang, L., Akerberg, B.N., Ma, Q., Li, K., He, A., Lin, Z., Stevens, S.M., Zhou, B., et al. (2017). Mapping cell type-specific transcriptional enhancers using high affinity, lineage-specific Ep300 bioChIP-seq. eLife *6*, e22039. https://doi.org/10.7554/eLife.22039.

20. Beckett, D., Kovaleva, E., and Schatz, P.J. (1999). A minimal peptide substrate in biotin holoenzyme synthetase-catalyzed biotinylation. Protein Sci. *8*, 921–929.

21. Jiao, K., Kulessa, H., Tompkins, K., Zhou, Y., Batts, L., Baldwin, H.S., and Hogan, B.L.M. (2003). An essential role of Bmp4 in the atrioventricular septation of the mouse heart. Genes Dev. *17*, 2362–2367.

22. Dai, Y.S., and Markham, B.E. (2001). p300 Functions as a coactivator of transcription factor GATA-4. J. Biol. Chem. *276*, 37178–37185.

23. He, J., Ye, J., Cai, Y., Riquelme, C., Liu, J.O., Liu, X., Han, A., and Chen, L. (2011). Structure of p300 bound to MEF2 on DNA reveals a mechanism of enhanceosome assembly. Nucleic Acids Res. *39*, 4464–4474.

24. Sartorelli, V., Huang, J., Hamamori, Y., and Kedes, L. (1997). Molecular mechanisms of myogenic coactivation by p300: direct interaction with the activation domain of MyoD and with the MADS box of MEF2C. Mol. Cell. Biol. *17*, 1010–1026.

25. Li, T., Li, Y.-M., Jia, Z.-Q., Chen, P., Ma, K.-T., and Zhou, C.-Y. (2007). Carboxyl terminus of Nkx2.5 impairs its interaction with p300. J. Mol. Biol. *370*, 976–992.

26. He, A., Kong, S.W., Ma, Q., and Pu, W.T. (2011). Co-occupancy by multiple cardiac transcription factors identifies transcriptional enhancers active in heart. Proc. Natl. Acad. Sci. USA *108*, 5632–5637.

27. VanDusen, N.J., Lee, J.Y., Gu, W., Butler, C.E., Sethi, I., Zheng, Y., King, J.S., Zhou, P., Suo, S., Guo, Y., et al. (2021). Author Correction: massively parallel in vivo CRISPR screening identifies RNF20/40 as epigenetic regulators of cardiomyocyte maturation. Nat. Commun. *12*, 5105.

28. Parikh, S.S., Blackwell, D.J., Gomez-Hurtado, N., Frisk, M., Wang, L., Kim, K., Dahl, C.P., Fiane, A., Tønnessen, T., Kryshtal, D.O., et al. (2017). Thyroid and glucocorticoid hormones promote functional T-tubule development in human-induced pluripotent stem cell-derived cardiomyocytes. Circ. Res. *121*, 1323–1330.

29. Arnold, C.D., Gerlach, D., Stelzer, C., Boryń, Ł.M., Rath, M., and Stark, A. (2013). Genome-wide quantitative enhancer activity maps identified by STARR-seq. Science *339*, 1074–1077.

30. Srivastava, D., and Olson, E.N. (2000). A genetic blueprint for cardiac development. Nature *407*, 221–226.

31. Sakamoto, T., Matsuura, T.R., Wan, S., Ryba, D.M., Kim, J.U., Won, K.J., Lai, L., Petucci, C., Petrenko, N., Musunuru, K., et al. (2020). A critical role for estrogen-related receptor signaling in cardiac maturation. Circ. Res. *126*, 1685–1702.

32. Han, P., Li, W., Lin, C.-H.H., Yang, J., Shang, C., Nuernberg, S.T., Jin, K.K., Xu, W., Lin, C.-Y.Y., Lin, C.-J.J., et al. (2014). A long noncoding RNA protects the heart from pathological hypertrophy. Nature *514*, 102–106.

33. Guo, Y., VanDusen, N.J., Zhang, L., Gu, W., Sethi, I., Guatimosim, S., Ma, Q., Jardin, B.D., Ai, Y., Zhang, D., et al. (2017). Analysis of cardiac myocyte maturation using CASAAV, a platform for rapid dissection of cardiac myocyte gene function in vivo. Circ. Res. *120*, 1874–1888.

34. Lieberman-Aiden, E., van Berkum, N.L., Williams, L., Imakaev, M., Ragoczy, T., Telling, A., Amit, I., Lajoie, B.R., Sabo, P.J., Dorschner, M.O., et al. (2009). Comprehensive mapping of long-range interactions reveals folding principles of the human genome. Science *326*, 289–293.

35. Rosa-Garrido, M., Chapski, D.J., Schmitt, A.D., Kimball, T.H., Karbassi, E., Monte, E., Balderas, E., Pellegrini, M., Shih, T.-T., Soehalim, E., et al. (2017). High-resolution mapping of chromatin conformation in cardiac myocytes reveals structural remodeling of the epigenome in heart failure. Circulation *136*, 1613–1625.

36. Sungalee, S., Liu, Y., Lambuta, R.A., Katanayeva, N., Donaldson Collier, M., Tavernari, D., Roulland, S., Ciriello, G., and Oricchio, E. (2021). Histone acetylation dynamics modulates chromatin conformation and allele-specific interactions at oncogenic loci. Nat. Genet. *53*, 650–662.

37. Wang, G., Meng, Q., Xia, B., Zhang, S., Lv, J., Zhao, D., Li, Y., Wang, X., Zhang, L., Cooke, J.P., et al. (2020). TADsplimer reveals splits and mergers of topologically associating domains for epigenetic regulation of transcription. Genome Biol. *21*, 84.

38. Fulco, C.P., Nasser, J., Jones, T.R., Munson, G., Bergman, D.T., Subramanian, V., Grossman, S.R., Anyoha, R., Doughty, B.R., Patwardhan, T.A., et al. (2019). Activity-by-contact model of enhancer-promoter regulation from thousands of CRISPR perturbations. Nat. Genet. *51*, 1664–1669.

39. Mumbach, M.R., Rubin, A.J., Flynn, R.A., Dai, C., Khavari, P.A., Greenleaf, W.J., and Chang, H.Y. (2016). HiChIP: efficient and sensitive analysis of protein-directed genome architecture. Nat. Methods *13*, 919–922.

40. Hnisz, D., Abraham, B.J., Lee, T.I., Lau, A., Saint-André, V., Sigova, A.A., Hoke, H.A., and Young, R.A. (2013). Super-enhancers in the control of cell identity and disease. Cell *155*, 934–947.

41. Man, J.C.K., Mohan, R.A., Boogaard, M.V.D., Hilvering, C.R.E., Jenkins, C., Wakker, V., Bianchi, V., Laat, W., Barnett, P., Boukens, B.J., et al. (2019). An enhancer cluster controls gene activity and topology of the SCN5A-SCN10A locus in vivo. Nat. Commun. *10*, 4943.

42. van den Boogaard, M., Wong, L.Y.E., Tessadori, F., Bakker, M.L., Dreizehnter, L.K., Wakker, V., Bezzina, C.R., 't Hoen, P.A.C., Bakkers, J., Barnett, P., et al. (2012). Genetic variation in T-box binding element functionally affects SCN5A/SCN10A enhancer. J. Clin. Invest. *122*, 2519–2530.

43. Rog-Zielinska, E.A., Thomson, A., Kenyon, C.J., Brownstein, D.G., Moran, C.M., Szumska, D., Michailidou, Z., Richardson, J., Owen, E., Watt, A., et al. (2013). Glucocorticoid receptor is required for foetal heart maturation. Hum. Mol. Genet. *22*, 3269–3282.

44. Cao, Y., Zhang, X., Akerberg, B.N., Yuan, H., Sakamoto, T., Xiao, F., VanDusen, N.J., Zhou, P., Sweat, M.E., Wang, Y., et al. (2023). In vivo dissection of chamber-selective enhancers reveals estrogen-related receptor as a regulator of ventricular cardiomyocyte identity. Circulation *147*, 881–896. https://doi.org/10.1161/CIRCULATIONAHA.122.061955.

45. Dowell, P., Ishmael, J.E., Avram, D., Peterson, V.J., Nevrivy, D.J., and Leid, M. (1997). p300 functions as a coactivator for the peroxisome proliferator-activated receptor alpha. J. Biol. Chem. *272*, 33435–33443.

46. Kuznetsova, T., Wang, S.-Y., Rao, N.A., Mandoli, A., Martens, J.H.A., Rother, N., Aartse, A., Groh, L., Janssen-Megens, E.M., Li, G., et al. (2015). Glucocorticoid receptor and nuclear factor kappa-B affect three-dimensional chromatin organization. Genome Biol. *16*, 264.

47. De Luca, A., Severino, A., De Paolis, P., Cottone, G., De Luca, L., De Falco, M., Porcellini, A., Volpe, M., and Condorelli, G. (2003). p300/cAMP-response-element-binding-protein ('CREB')-binding protein (CBP) modulates co-operation between myocyte enhancer factor 2A (MEF2A) and thyroid hormone receptor-retinoid X receptor. Biochem. J. *369*, 477–484.

48. Lupiáñez, D.G., Kraft, K., Heinrich, V., Krawitz, P., Brancati, F., Klopocki, E., Horn, D., Kayserili, H., Opitz, J.M., Laxova, R., et al. (2015). Disruptions of topological chromatin domains cause pathogenic rewiring of gene-enhancer interactions. Cell *161*, 1012–1025.

49. Stadhouders, R., Vidal, E., Serra, F., Di Stefano, B., Le Dily, F., Quilez, J., Gomez, A., Collombet, S., Berenguer, C., Cuartero, Y., et al. (2018). Transcription factors orchestrate dynamic interplay between genome topology and gene regulation during cell reprogramming. Nat. Genet. *50*, 238–249.

50. Wang, R., Chen, F., Chen, Q., Wan, X., Shi, M., Chen, A.K., Ma, Z., Li, G., Wang, M., Ying, Y., et al. (2022). MyoD is a 3D genome structure organizer for muscle cell identity. Nat. Commun. *13*, 205.

51. Dixon, J.R., Selvaraj, S., Yue, F., Kim, A., Li, Y., Shen, Y., Hu, M., Liu, J.S., and Ren, B. (2012). Topological domains in mammalian genomes identified by analysis of chromatin interactions. Nature *485*, 376–380.

52. He, A., Gu, F., Hu, Y., Ma, Q., Ye, L.Y., Akiyama, J.A., Visel, A., Pennacchio, L.A., and Pu, W.T. (2014). Dynamic GATA4 enhancers shape the chromatin landscape central to heart development and disease. Nat. Commun. *5*, 4907.

53. Bolger, A.M., Lohse, M., and Usadel, B. (2014). Trimmomatic: a flexible trimmer for Illumina sequence data. Bioinformatics *30*, 2114–2120.

54. Langmead, B., and Salzberg, S.L. (2012). Fast gapped-read alignment with Bowtie 2. Nat. Methods *9*, 357–359.

55. Li, H., Handsaker, B., Wysoker, A., Fennell, T., Ruan, J., Homer, N., Marth, G., Abecasis, G., and Durbin, R.; 1000 Genome Project Data Processing Subgroup (2009). The Sequence Alignment/Map format and SAMtools. Bioinformatics *25*, 2078–2079.

56. Quinlan, A.R., and Hall, I.M. (2010). BEDTools: a flexible suite of utilities for comparing genomic features. Bioinformatics *26*, 841–842.

57. Zhang, Y., Liu, T., Meyer, C.A., Eeckhoute, J., Johnson, D.S., Bernstein, B.E., Nusbaum, C., Myers, R.M., Brown, M., Li, W., et al. (2008). Model-based analysis of ChIP-Seq (MACS). Genome Biol. *9*, R137.

58. Shen, L., Shao, N., Liu, X., and Nestler, E. (2014). ngs.plot: quick mining and visualization of next-generation sequencing data by integrating genomic databases. BMC Genomics *15*, 284.

59. Ross-Innes, C.S., Stark, R., Teschendorff, A.E., Holmes, K.A., Ali, H.R., Dunning, M.J., Brown, G.D., Gojis, O., Ellis, I.O., Green, A.R., et al. (2012). Differential oestrogen receptor binding is associated with clinical outcome in breast cancer. Nature *481*, 389–393.

60. Heinz, S., Benner, C., Spann, N., Bertolino, E., Lin, Y.C., Laslo, P., Cheng, J.X., Murre, C., Singh, H., and Glass, C.K. (2010). Simple combinations of lineage-determining transcription factors prime cis-regulatory elements required for macrophage and B cell identities. Mol. Cell *38*, 576–589.

61. Parks, D.H., Tyson, G.W., Hugenholtz, P., and Beiko, R.G. (2014). STAMP: statistical analysis of taxonomic and functional profiles. Bioinformatics *30*, 3123–3124.

62. Ramírez, F., Ryan, D.P., Grüning, B., Bhardwaj, V., Kilpert, F., Richter, A.S., Heyne, S., Dündar, F., and Manke, T. (2016). deepTools2: a next generation web server for deep-sequencing data analysis. Nucleic Acids Res. *44*, W160–W165.

63. Dobin, A., Davis, C.A., Schlesinger, F., Drenkow, J., Zaleski, C., Jha, S., Batut, P., Chaisson, M., and Gingeras, T.R. (2013). STAR: ultrafast universal RNA-seq aligner. Bioinformatics *29*, 15–21.

64. Putri, G.H., Anders, S., Pyl, P.T., Pimanda, J.E., and Zanini, F. (2022). Analysing high-throughput sequencing data in Python with HTSeq 2.0. Bioinformatics *38*, 2943–2945.

65. Love, M.I., Huber, W., and Anders, S. (2014). Moderated estimation of fold change and dispersion for RNA-seq data with DESeq2. Genome Biol. *15*, 550.

66. Yu, G., Wang, L.-G., Han, Y., and He, Q.-Y. (2012). clusterProfiler: an R package for comparing biological themes among gene clusters. Omics *16*, 284–287.

67. Durand, N.C., Shamim, M.S., Machol, I., Rao, S.S.P., Huntley, M.H., Lander, E.S., and Aiden, E.L. (2016). Juicer provides a one-click system for analyzing loop-resolution Hi-C experiments. Cell Syst. *3*, 95–98.

68. Abdennur, N., and Mirny, L.A. (2020). Cooler: scalable storage for Hi-C data and other genomically labeled arrays. Bioinformatics *36*, 311–316.

69. Open2C, Abdennur, N., Abraham, S., Fudenberg, G., Flyamer, I.M., Galitsyna, A.A., Goloborodko, A., Imakaev, M., Oksuz, B.A., and Venev, S.V. (2022). Cooltools: enabling high-resolution Hi-C analysis in Python. https://doi.org/10.1101/2022.10.31.514564.

70. Rowley, M.J., Poulet, A., Nichols, M.H., Bixler, B.J., Sanborn, A.L., Brouhard, E.A., Hermetz, K., Linsenbaum, H., Csankovszki, G., Lieberman Aiden, E., et al. (2020). Analysis of Hi-C data using SIP effectively identifies loops in organisms from C. elegans to mammals. Genome Res. *30*, 447–458.

71. Durand, N.C., Robinson, J.T., Shamim, M.S., Machol, I., Mesirov, J.P., Lander, E.S., and Aiden, E.L. (2016). Juicebox provides a visualization system for Hi-C contact maps with unlimited zoom. Cell Syst. *3*, 99–101.

72. Servant, N., Varoquaux, N., Lajoie, B.R., Viara, E., Chen, C.-J., Vert, J.-P., Heard, E., Dekker, J., and Barillot, E. (2015). HiC-Pro: an optimized and flexible pipeline for Hi-C data processing. Genome Biol. *16*, 259.

73. Lareau, C.A., and Aryee, M.J. (2018). hichipper: a preprocessing pipeline for calling DNA loops from HiChIP data. Nat. Methods *15*, 155–156.

74. Phanstiel, D.H., Boyle, A.P., Heidari, N., and Snyder, M.P. (2015). Mango: a bias-correcting ChIA-PET analysis pipeline. Bioinformatics *31*, 3092–3098.

75. Lareau, C.A., and Aryee, M.J. (2018). diffloop: a computational framework for identifying and analyzing differential DNA loops from sequencing data. Bioinformatics *34*, 672–674.

76. Wang, S., Guo, Y., and Pu, W.T. (2021). AAV gene transfer to the heart. Methods Mol. Biol. *2158*, 269–280.

77. Clement, K., Rees, H., Canver, M.C., Gehrke, J.M., Farouni, R., Hsu, J.Y., Cole, M.A., Liu, D.R., Joung, J.K., Bauer, D.E., et al. (2019). CRISPResso2 provides accurate and rapid genome editing sequence analysis. Nat. Biotechnol. *37*, 224–226.

78. Langmead, B., Trapnell, C., Pop, M., and Salzberg, S.L. (2009). Ultrafast and memory-efficient alignment of short DNA sequences to the human genome. Genome Biol. *10*, R25.

79. Jolma, A., Yin, Y., Nitta, K.R., Dave, K., Popov, A., Taipale, M., Enge, M., Kivioja, T., Morgunova, E., and Taipale, J. (2015). DNA-dependent formation of transcription factor pairs alters their binding specificity. Nature *527*, 384–388.

80. Mahony, S., Auron, P.E., and Benos, P.V. (2007). DNA familial binding profiles made easy: comparison of various motif alignment and clustering strategies. PLoS Comput. Biol. *3*, e61.

81. Siepel, A., Bejerano, G., Pedersen, J.S., Hinrichs, A.S., Hou, M., Rosenbloom, K., Clawson, H., Spieth, J., Hillier, L.W., Richards, S., et al. (2005). Evolutionarily conserved elements in vertebrate, insect, worm, and yeast genomes. Genome Res. *15*, 1034–1050.

82. Chen, K., Xi, Y., Pan, X., Li, Z., Kaestner, K., Tyler, J., Dent, S., He, X., and Li, W. (2013). DANPOS: dynamic analysis of nucleosome position and occupancy by sequencing. Genome Res. *23*, 341–351.

83. Anders, S., Pyl, P.T., and Huber, W. (2015). HTSeq–a Python framework to work with high-throughput sequencing data. Bioinformatics *31*, 166–169.

84. Open2C, Abdennur, N., Abraham, S., Fudenberg, G., Flyamer, I.M., Galitsyna, A.A., Goloborodko, A., Imakaev, M., Oksuz, B.A., and Venev, S.V. (2022). Cooltools: enabling high-resolution Hi-C analysis in Python. https://doi.org/10.1101/2022.10.31.514564.

85. Li, H., and Durbin, R. (2010). Fast and accurate long-read alignment with Burrows–Wheeler transform. Bioinformatics *26*, 589–595.

86. Song, F., Xu, J., Dixon, J., and Yue, F. (2022). Analysis of Hi-C data for discovery of structural variations in cancer. Methods Mol. Biol. *2301*, 143–161.

87. Lovén, J., Hoke, H.A., Lin, C.Y., Lau, A., Orlando, D.A., Vakoc, C.R., Bradner, J.E., Lee, T.I., and Young, R.A. (2013). Selective inhibition of tumor oncogenes by disruption of super-enhancers. Cell *153*, 320–334.

88. Whyte, W.A., Orlando, D.A., Hnisz, D., Abraham, B.J., Lin, C.Y., Kagey, M.H., Rahl, P.B., Lee, T.I., and Young, R.A. (2013). Master transcription factors and mediator establish super-enhancers at key cell identity genes. Cell *153*, 307–319.

89. Robinson, J.T., Thorvaldsdóttir, H., Winckler, W., Guttman, M., Lander, E.S., Getz, G., and Mesirov, J.P. (2011). Integrative genomics viewer. Nat. Biotechnol. *29*, 24–26.

90. Li, D., Harrison, J.K., Purushotham, D., and Wang, T. (2022). Exploring genomic data coupled with 3D chromatin structures using the WashU epigenome Browser. Nat. Methods *19*, 909–910.

Please cite this article in press as: Zhou et al., Dynamic changes in P300 enhancers and enhancer-promoter contacts control mouse cardiomyocyte maturation, Developmental Cell (2023), https://doi.org/10.1016/j.devcel.2023.03.020

STAR★METHODS

KEY RESOURCES TABLE

REAGENT or RESOURCE	SOURCE	IDENTIFIER
Antibodies		
Rabbit polyclonal anti-P300	Santa Cruz	sc-585; RRID: AB_2231120
Chicken polyclonal anti-BirA	Abcam	ab14002; RRID: AB_300830
Goat polyclonal to Cardiac Troponin I	Abcam	ab56357; RRID: AB_880622
Bacterial and virus strains		
SURE Electrocompetent cells	Agilent	200227
scAAV-Enh-Mlc2v-mCherry (MPRA and individual enhancer testing)	Addgene	182649
scAAV-Hsp68-mCherry (MPRA vector)	Addgene	195412
Biological samples		
Maturation MPRA: AAV DNA	This paper	GEO: GSM5876202-GSM5876204
Maturation MPRA: E15.5 injection, P0 collection of RNA from ventricles	This paper	GEO: GSM5876205-GSM5876216
Maturation MPRA: P0 injection, P7 collection of RNA from ventricles	This paper	GEO: GSM5876217-GSM5876244
Maturation MPRA: P0 injection, P28 collection of RNA from ventricles	This paper	GEO: GSM5876245-GSM5876272
Nuclear Receptor MPRA: AAV DNA	This paper	GEO: GSM5876185-GSM5876187
Nuclear Receptor MPRA: P0 injection, P7 collection of RNA from ventricles	This paper	GEO: GSM5876188-GSM5876201
E12.5, E16.5, P0, P7, P14, P28, and P42 mouse ventricles for P300 bioChIP-seq	This paper	N/A
E12.5, P0, and P42 mouse ventricular CMs for Hi-C	This paper	N/A
E12.5, E16.5, P0, P7, P14, P28, and P42 mouse ventricular CMs for for bulk RNA-seq	This paper	N/A
E12.5 and P42 mouse ventricular CMs for H3K27ac Hi-ChIP	This paper	N/A
Critical commercial assays		
Dynabeads M-280 Streptavidin	ThermoFisher Scientific	11205D
KAPA Hyper Prep Kit	Kapa Biosystems	KK8502
Mouse neonatal CM isolation kit	Miltenyi Biotec	130-100-825
Ribo-Zero Plus rRNA Depletion Kit	Illumina	20040526
TruSeq RNA Library Prep Kit v2	Illumina	RS-122-2001
Arima-HiC+ kit for HiChIP	Arima Genomics	201911-792
Experimental models: Organisms/strains		
p300-flbio;Rosa26^{BirA}	The Jackson Laboratory	025980
Rosa26^{fsTRAP}	The Jackson Laboratory	022367
Rosa26^{fsBirA}	Derived from Rosa26^{fsTRAP}	N/A
B6J.129(B6N)-Gt(ROSA)26Sortm1(CAG-cas9*,-EGFP)Fezh/J mice	The Jackson Laboratory	026175
Myh7^{YFP} mice	UNC-CH/Oliver Smithies	N/A
Swiss Webster (CFW) mice	Charles River	024
Oligonucleotides		
Oligo pool libraries for MPRA	Agilent SurePrint	N/A
A full list of oligos and primers in Table S1	This paper	N/A

(*Continued on next page*)

Please cite this article in press as: Zhou et al., Dynamic changes in P300 enhancers and enhancer-promoter contacts control mouse cardiomyocyte maturation, Developmental Cell (2023), https://doi.org/10.1016/j.devcel.2023.03.020

Continued

REAGENT or RESOURCE	SOURCE	IDENTIFIER
Deposited data		
P300 bioChIP-seq of E12.5-P42 murine CMs	This paper	GEO: GSE195901
Bulk RNA-seq of E12.5-P42 murine CMs	This paper	GEO: GSE195902
Hi-C of E12.5, P0, and P42 murine CMs	This paper	GEO: GSE194087
H3K27ac HiChIP of E12.5 and P42 murine CMs	This paper	GEO: GSE222160
Massively parallel reporter assay of P300 enhancers	This paper	GEO: GSE196346
Massively parallel reporter assay of nuclear receptor-containing enhancers	This paper	GEO: GSE196346
ChIP-seq of Mef2A, Mef2C, Nkx2-5, Tbx5, Tead1 in fetal and adult murine heart ventricles	Akerberg et al.[15]	GEO: GSE124008
ChIP-seq of GATA4 in fetal and adult murine heart ventricles.	He et al.[52]	GEO: GSE52123
THRA ChIP-seq of P15 murine hearts	Hirose et al.[8]	GEO: GSE125414
P300 ChIP-seq of E12.5 murine forebrains and hearts, H3K27ac ChIP-seq of E12.5 murine hearts.	Zhou et al.[19]	GEO: GSE88789
Uncropped western blots	This paper	https://figshare.com/articles/figure/Uncropped_WB_Fig_1B_pdf/22250587
Software		
Trimmomatic/0.36	Bolget et al.[53]	http://www.usadellab.org/cms/index.php?page=trimmomatic
Bowtie2/2.3.4.3	Langmead and Salzberg[54]	bowtie-bio.sourceforge.net/bowtie2
Samtools/1.9	Li et al.[55]	http://www.htslib.org/
Bedtools/2.27.1	Quinlan and Hall[56]	bedtools.readthedocs.io
MACS2	Zhang et al.[57]	https://pypi.org/project/MACS2/
ngs.plot	Shen et al.[58]	https://github.com/shenlab-sinai/ngsplot
diffbind	Ross-Innes et al.[59]	https://bioconductor.org/packages/release/bioc/html/DiffBind.html
Homer	Heinz et al.[60]	http://homer.ucsd.edu/homer/
STAMP	Parks et al.[61]	https://beikolab.cs.dal.ca/software/STAMP
deeptools	Ramierez et al.[62]	https://deeptools.readthedocs.io/en/develop/
STAR	Dobin et al.[63]	https://github.com/alexdobin/STAR
HTSeq-count	Putri et al.[64]	https://htseq.readthedocs.io/en/release_0.11.1/index.html
DESeq2	Love et al.[65]	https://bioconductor.org/packages/release/bioc/html/DESeq2.html
ClusterProfiler	Yu et al.[66]	https://guangchuangyu.github.io/software/clusterProfiler/
Juicer v2.0	Durand[67]	https://github.com/aidenlab/juicer
Cooler v0.8.11	Abdennur and Mirny[68]	https://github.com/open2c/cooler
cooltools v0.5.0	Open2c[69]	https://github.com/open2c/cooltools
SIP v1.6.1	Rowley et al.[70]	https://github.com/PouletAxel/SIP
TADsplimer v1.1	Wang et al.[37]	https://github.com/GuangyWang/TADsplimer
Juicebox v1.9.8	Durand et al.[71]	https://github.com/aidenlab/Juicebox
HiC-Pro v3.1.0	Servant et al.[72]	https://github.com/nservant/HiC-Pro
hichipper v0.7.7	Lareau et al.[73]	https://github.com/aryeelab/hichipper
mango	Phanstiel et al.[74]	https://github.com/dphansti/mango
diffloop	Lareau et al.[75]	https://github.com/aryeelab/diffloop
ABC score calculation	This paper	https://github.com/yanchunzhang/Cardiomyocyte_maturation_HiC

Please cite this article in press as: Zhou et al., Dynamic changes in P300 enhancers and enhancer-promoter contacts control mouse cardiomyocyte maturation, Developmental Cell (2023), https://doi.org/10.1016/j.devcel.2023.03.020

RESOURCE AVAILABILITY

Lead contact

Further information and requests for resources and reagents should be directed to the lead contact William Pu (william.pu@cardio.chboston.org).

Materials availability

Key Plasmids have been deposited to Addgene. Mice are available from public repositories. Other unique materials and reagents generated in this study are available upon request from the lead contact with a completed Materials Transfer Agreement.

Data and code availability

The following public data sources were used for this study: E12.5_heart_P300_bioChIP-seq, E12.5_forebrain_P300_bioChIP-seq, adult_heart_P300_bioChIP-seq and adult_heart-EC_P300_bioChIP-seq data are from GSE88789[19]; GATA4 bioChIP-seq data of E12.5 or adult heart apex are from GSE52123[52]; Mef2a, Mef2c, Nkx2-5, SRF, Tbx5, and Tead1 bioChIP-seq data of E12.5 or adult heart apex are from GSE124008.[15] Original data in this manuscript including P300 bioChIP-seq, bulk RNA-seq, Hi-C and H3K27ac HiChIP data of mouse CMs have been deposited to gene expression omnibus SuperSeries GSE195905.

The custom scripts used in this study are publicly available on github (https://github.com/yanchunzhang/Cardiomyocyte_maturation_HiC). https://doi.org/10.5281/zenodo.7716979.

Additional information required to reanalyze the data reported in this paper is available from the lead contact upon request.

EXPERIMENTAL MODEL AND SUBJECT DETAILS

Mice

All mouse experiments were performed under protocols approved by the Boston Children's Hospital Institutional Animal Care and Use Committee. $P300^{flbio}$ (Jax #025980), Tnnt2-Cre (Jax #024240), Myh6-Cre (Jax #011038), $Rosa26^{mTmG}$ (Jax #007576) and Cdh5 (Pac)-CreERT2 (Taconic #13073) have been previously described. $Rosa26^{fsBirA}$ was derived from the $Rosa26^{fsTRAP}$ (Jax #022367) mouse by removal of the frt-TRAP-frt cassette using germline Flp recombination.[19] Mice were on a C57BL6/129 mixed background. Mixed genetic background mice or Swiss Webster outbred mice were used for AAV injection. Male and female mice were pooled for all assays. Mice were housed in a specific pathogen free facility with 12 hour light and dark cycles.

Intracardiac fetal injections were performed on anesthetized pregnant dams. Portions of the uterus were externalized through a midline abdominal incision. A pulled glass needle was advanced through the uterine wall and the back of the embryo into the heart. Virus was then injected and the needle withdrawn. After injection of multiple embryos, the uterus was returned to the embryo and the abdominal wall was sutured in layers.

METHOD DETAILS

Cardiomyocyte isolation and purification

For E12.5, E16.5, P0, and P7 CMs, ventricular apexes were dissociated using the Neonatal mouse CM isolation kit (Cellutron Life Technologies) and purified using the mouse neonatal CM isolation kit (Miltenyi). P14, P28, and P42 CMs were dissociated and purified from ventricular apexes by Langendorf collagenase perfusion followed by differential sedimentation as described.[6] CM preparations were over 90% pure as determined by examining CMs purified from $Rosa26^{mTmG/+}$;Tnnt2-Cre+ mice with fluorescence microscopy. Purified CMs were used with three biological replicates per group for Hi-C and RNA-seq.

P300 pulldown for Western Blot

For streptavidin pulldown of $P300^{flbio}$ from P7 hearts, *$p300^{flbio/+}$; $Rosa26^{fsBirA/+}$;Myh6-Cre+* heart ventricles were homogenized in cold PBS and protein lysate was prepared with 0.5% SDS lysis buffer (1xPBS supplemented with 1 mM DTT, protease inhibitor cocktail, and 0.5% SDS). Biotinylated proteins were then pulled down by incubating with Dynabeads M-280 streptavidin (ThermoFisher Scientific, Cat#11206D) at 4°C for one hour. After washing at room temperature 5 times for 5 minutes each with PBS supplemented with 0.2% SDS, bound proteins were eluted from the beads with SDS elution buffer (20 mM Tris-HCl pH 8.0, 1% SDS, and 2 mM ETDA) at 98°C for 10 minutes. Western blotting was performed using standard protocols and antibodies against P300 (Santa Cruz, sc-585) and BirA (Abcam, ab14002).

Immunostaining

Cryosections of E12.5 embryos and P0 hearts were stained with cardiac troponin I (TNNI3, Abcam, ab56357) and imaged by confocal microscopy (Olympus FV3000).

P300 bioChIP-seq of cardiomyocytes

P300 bioChIP-seq was performed as described previously.[19] E12.5 to P42 heart ventricles were harvested, homogenized, and cross-linked in 1% formaldehyde in PBS for 10 minutes at room temperature and subsequently quenched with 125 mM glycine for 5 min.

Chromatin was fragmented using a microtip sonicator (Qsonica, S-3000) at 30% amplitude for 8 minutes. Biotinylated P300 and bound chromatin was pulled down by incubation with streptavidin beads (ThermoFisher Scientific, 11206D). Bead-bound chromatin was resuspended in SDS elution buffer (50 mM Tris–HCl pH 8,10 mM EDTA, 1% SDS) and incubated overnight at 65 °C to reverse crosslinking. After RNAse A and Proteinase K treatment, ChIP DNA was purified using Qiagen MinElute columns. Libraries were constructed using the KAPA HyperPrep ChIP-seq library preparation kit (Roche, cat# 07962347001). Sequencing (75 nt single end) was performed on an Illumina NextSeq 500.

AAV reporter assays

Wild type or mutant genomic regions were PCR amplified or synthesized (sequences listed in Table S1) and cloned into a self-complementary adeno-associated virus (scAAV) mCherry reporter vector. Adeno-associated virus serotype 9 (AAV9) was generated as described.[76] Briefly, HEK293T cells were transfected with ITR plasmid, rep-cap plasmid, and helper plasmid. AAV was purified using OptiPrep density gradient purification (Sigma). Purified virus was delivered to E15.5 embryos by transuterine intracardiac injection (5E10 viral genomes/embryo), or subcutaneous injection in P0 pups (2E11 viral genomes/g body weight). Heart ventricles were collected for RNA and DNA at P0, P7, or P28. RNA was extracted using TRIzol (Life Technologies) and purified with Zymo RNA Clean kit. Viral DNA was recovered with DirectPCR lysis reagent (Viagen, Cat#101-T). Reporter activity was determined by the ratio of mCherry RNA/DNA, normalized to *Rplp0* and control genomic regions, respectively.

Massively parallel reporter assay (MPRA)

Enhancers were synthesized by Agilent as an oligonucleotide pool. Each enhancer consisted of two 230 bp single stranded DNA oligos with 20 bp 3′ overlap. Each oligonucleotide's 5′ end had a 20 bp primer-binding site. Oligonucleotides within the pool were annealed and 3′ ends were extended by PCR to create a library of 400 bp enhancers flanked by 20 bp priming sites. NotI/AscI-restriction sites were added to enhancers in a second round of PCR. The enhancer library was then digested, size selected, and ligated into the multiple cloning site of a self-complementary AAV plasmid containing minimal promoter-mCherry-NotI/AscI-polyA sequences (Addgene #182649). The ligation product was electroporated into Agilent SURE Electrocompetent cells following manufacturer recommendations, spread onto agar plates, and cultured overnight. Approximately 900,000 colonies were harvested and pooled for plasmid maxi-prep. The MPRA library was packaged into AAV9 as described above.

For enhancer activity measurement at P0, AAV9-MPRA library was delivered to wild type CFW E15.5 embryos (5E10 viral genomes/embryo, n=12) by intracardiac injection. Heart ventricles were harvested at P0. For enhancer activity at P7 and P28, AAV9-MPRA library was injected subcutaneously to P0 pups (2E11 viral genomes/g). Hearts were harvested at P7 (n=28) or P28 (n=28). For nuclear receptor WT-Mut pairs, 190 bp regions centered on a candidate nuclear receptor motif and flanked by 20 bp priming sites, were synthesized as a pool (Agilent) and cloned into the AAV9-MPRA vector. NR motifs were mutated by shuffling their DNA sequence and rescanning to confirm loss of the motif. AAV9-MPRA library was injected subcutaneously to P0 pups (2E11 viral genomes/g) and harvested at P7 (n=14).

RNA was isolated from homogenized ventricular apexes via TRIzol extraction and reverse transcribed using a primer recognizing the start of the polyA sequence. NGS adapters and unique indexes were added to each sample in subsequent rounds of PCR amplification. Untransduced AAV DNA from the library pool was also prepared in the same fashion for sequencing in triplicate. Indexed samples were pooled and paired-end (2 × 150 bp) sequenced on a NextSeq500. After removal of adapters,[53] reads were aligned to the mouse genome,[54,55] keeping only mates that produced concordant alignments between 395 and 405 bp. On average, each sample contained ~5M alignments passing these criteria. The number of reads for each enhancer in each sample was determined using BedTools.[56] The average number of reads for each enhancer within the untransduced AAV DNA was then calculated, and enhancers present at low frequencies (<5 RPM) were excluded. The majority (>90%) of enhancers were successfully created and were detected above the 5 RPM threshold. Read numbers for RNA samples was determined using the same method. RNA:DNA ratio for each region was calculated and used as a readout of enhancer activity.

Regions were defined as "active" when their RNA;DNA ratio exceeded the 95th percentile for the negative control regions. This is a relatively conservative definition of activity, since some negative control regions had relatively high RNA:DNA ratio.

Amplicon-sequencing of somatic mutagenesis target site

Newborn *Rosa26*^{fsCas9}; *Myh7*^{YFP} mice were transduced with a mosaic dose of AAV vector carrying Tnnt2-Cre and a gRNA (ACATTGGGTCAGCTTGGGTC) targeting a nuclear receptor motif within the *Mhrt* promoter. CMs were collected at P28 and genomic DNA was isolated. A 16 bp UMI and partial NGS adapter fused to primers flanking the cut site were added in a single PCR cycle, followed by 25 cycles of amplification which added full length NGS adapters. Three amplicon replicates were paired-end sequenced (2x150 bp) to an average depth of ~1.7M reads per replicate. Read pairs were merged using Paired-End reAd mergeR (PEAR), deduplicated by UMI using AmpUMI, and the distribution of mutations was analyzed via CRISPResso2.[77]

Hi-C with mouse cardiomyocytes

Hi-C was performed as described.[10] For each biological replicate, 2M purified CMs were fixed in PBS supplemented with 1% formaldehyde for 10 min at RT and then quenched with 125 mM glycine for 5 min at RT. Nuclei were isolated by treating with a hypotonic buffer (10 mM Tris-HCl, pH 8.0, 10 mM KCl, 1 mM $MgCl_2$, 0.2% Igepal CA630) on ice for 10 min. Pelleted nuclei were permeabilized using 0.5% SDS and incubated for 10 min at 62 °C. Chromatin was digested using the 4-base cutter restriction enzyme MboI (200

Please cite this article in press as: Zhou et al., Dynamic changes in P300 enhancers and enhancer-promoter contacts control mouse cardiomyocyte maturation, Developmental Cell (2023), https://doi.org/10.1016/j.devcel.2023.03.020

units, NEB) at 37 °C overnight. After inactivation of MboI for 20 min at 62 °C, single stranded overhangs were filled with biotinylated-14-dATP (Life Technologies) and dCTP, dGTP, and dTTP using Klenow DNA polymerase (40 units, NEB) for 90 min at 37 °C. DNA was then ligated for 4 h at 16 °C using T4 DNA ligase (2,000 units, NEB). Reverse crosslinking was performed by incubating at 55 °C with proteinase K for 30 min and then 68 °C overnight. Purified DNA was sonicated using an ultra sonicator to 300–700 bp small fragments. After size selection and purification using SPRI beads (Beckman Coulter), biotinylated DNA was isolated using Dynabeads MyOne T1 Streptavidin beads (Life Technologies). Sequencing libraries were prepared on magnetic beads and final PCR amplification was carried out for 6 cycles. Size distribution of bead-purified libraries was checked using a High Sensitivity D1000 ScreenTape on a Tapestation (Agilent) and quantified using Qubit (Life Technologies). Libraries were sequenced on Hiseq 4000 (100 bp PE, Illumina). More than 70% of the *cis* reads were long-range (>20 kb) intra-chromosomal interactions.

H3K27ac HiChIP of mouse cardiomyocytes

H3K27ac HiChIP libraries were prepared using the Arima HiC+ kit (Arima Genomics). Briefly, ~2 M purified CMs were crosslinked with 2% formaldehyde for 10 min at room temperature. Crosslinked chromatin was digested using the Arima proprietary restriction enzyme cocktail. The fragmented chromatin ends were then filled in with a biotinylated nucleotide. Spatially proximal fragmented ends were ligated. Subsequently, chromatin was fragmented using a QSonica Q800R3 sonicator and incubated with H3K27ac antibody (Catalog No: 39133, Active Motif) at 4 °C overnight. The antibody-bound chromatin was immunoprecipitated using Protein A magnetic beads (Invitrogen) and reverse crosslinked using Arima-HiC+ kit reagents. Sequencing adapters and indexing primers were added using the Swift Biosciences Accel-NGS 2S Plus DNA Library Kit. The libraries were quantified to determine the appropriate number of PCR cycles needed for library amplification using the KAPA Library Quantification Kit (Roche) and then amplified using the KAPA Library Amplification Kit (Roche).

Cardiomyocyte RNA-Seq

RNA was purified using the Purelink RNA mini kit (Life Technologies). Ribosomal RNA was depleted using Ribo-Zero rRNA removal kits (Epicentre). RNA-seq libraries were prepared using ScriptSeq v2 library kit (Epicentre). Libraries were sequenced using an Illumina NextSeq500 with single end 75 bp reads. At least 50 M reads were obtained for each biological replicate.

ChIP-seq data analysis

The raw reads from bioChIP-Seq datasets were mapped to the Mus musculus genome (mm10 build) using Bowtie[78] v1.1.1. Alignments with more than one match were removed. MACS2[57] was used to determine peaks in each replicate with p-value 1e-5 as cutoff. The peak list was further filtered to remove all blacklisted regions (as defined by ENCODE for mm10 ChIP-Seq: http://mitra.stanford.edu/kundaje/akundaje/release/blacklists/mm10-mouse/).

The intersection of peaks from the replicates at each time point yielded the reproducible peaks. The intersection and union sets were determined by the Bedtools[56] intersect function. Profile and heatmap plot were generated by ngs.plot.[58] To define dynamic P300 regions, Diffbind[59] was used to normalize across samples. Peaks with significant signal in at least two time points were ranked by the ratio of their maximum to minimum values, and classified as described in Figure 2A. Motifs were determined by scanning a 200 bp window centered on the summits of peaks for all possible matches to a reference PWM file using Homer.[60] The reference PWM file was generated from the union of the default motifs provided with Homer and experimentally determined TF heterodimer motifs defined as reported.[79] The motifs were then clustered based on their similarity to each other using STAMP[80] and highly redundant motifs were removed.

Characterization of P300 enhancer regions

Conservation of regions was analyzed using precalculated phastCons 60-way vertebrate scores.[81] The profiles of dynamic/static P300 enhancer regions were generated by computeMatrix and plotProfile commands from DeepTools.[62] P300 signals were quantile-normalized using Danpos2[82] for comparison between stages.

We evaluated the specificity, sensitivity, and accuracy of P300-occupied regions compared to cardiac enhancer activity experimentally measured by transient transgenesis and compiled in the Vista enhancer database.[18] Mouse genomic regions tested in Vista were classified using the database entries into those with or without cardiac activity (cardiac$^+$, cardiac$^-$), where cardiac activity indicates transgene expression in any portion of the heart. These regions were also classified based on P300 occupancy (P300$^+$, P300$^-$). Sensitivity is cardiac$^+$;P300$^+$ / [cardiac$^+$;P300$^+$ + cardiac+;P300$^-$]. Specificity is cardiac$^-$;P300$^-$ / [cardiac$^-$;P300$^+$ + cardiac$^-$;P300$^-$]. Accuracy is [cardiac$^+$;P300$^+$ + cardiac$^-$;P300$^-$] / [cardiac$^+$ + cardiac$^-$].

RNA-seq data analysis

Raw reads were mapped to the mm10 reference genome using STAR.[63] Raw read counts of all genes were generated by HTseq-count.[83] Differential expressed genes (DEGs) were identified by DEseq2.[65] For DEGs between E12.5 and P42, cutoffs were set as absolute $\log_2$FC >=1 and $P_{adj} < 0.05$. For DEG heatmap between embryonic stages and adult stages, all replicates of E12.5 and E16.5 were pooled as embryonic and all replicates of P28 and P42 were pooled as adult, with cutoffs as absolute $\log_2$FC >=3 and $P_{adj} < 0.01$. Heatmap of DEGs was generated by R package pheatmap. Gene ontology enrichment analysis was done by R package ClusterProfiler.[66]

Please cite this article in press as: Zhou et al., Dynamic changes in P300 enhancers and enhancer-promoter contacts control mouse cardiomyocyte maturation, Developmental Cell (2023), https://doi.org/10.1016/j.devcel.2023.03.020

Hi-C data analysis

Raw reads were mapped with Juicer v2.0[67] to mm10 reference genome with default parameters. Then the paired mapped reads with mapping quality no less than 30 were binned and converted into.cool files by Cooler v0.8.11.[68] KR balancing was applied to the.cool file by cooler balance commands. Expected contact matrix at different distances was calculated by cooltools v0.5.0[84] expected-cis command.

Compartment scores were calculated by cooltools eigs-cis command at 100 kb resolution. Then compartment scores were calibrated by GC content and defined as compartment A or B, according to higher or lower GC content. Principal component analysis was implemented by R prcomp function on the whole-genome compartment scores of all replicates to check the reproducibility of replicates. Then replicates were merged into one combined.cool file for further analysis.

Loops were called by SIP v1.6.1[70] at 5 kb and 10 kb resolutions. Then loops from different stages were pooled together for further analysis. Loops were defined as enhancer-promoter (E-P) loops when at least one P300 enhancer located at one anchor of the loop and at least one TSS located at another anchor of the loop. For all E-P loops, the observed/expected value at loop center was deemed as the intensity of the loop.

TAD and TAD split events were defined by TADsplimer v1.1[37] at 10 kb resolution with default parameters. TAD insulation scores were calculated by cooltools diamond with 500 kb window at resolution of 5kb. For all TAD split events, the fold change of the intensity of P300 signal or gene expression level was calculated as the intensity of the stronger side of split sites divided by the intensity of the weaker side. Visualization of contact matrixes was performed using python modules cooltools+matplotlib or Juicebox v1.9.8.[67]

To plot the relationship between a region's distance to TSS and its TSS contact frequency, aggregated intra-chromosomal contact score at each distance (in 5 kb bins) was summed then divided by the total intra-chromosomal contact score. The curve was plotted as a cumulative distribution function.

H3K27ac HiChIP data analysis

Raw sequencing reads were mapped to mm10 reference genome using the HiChIP pipeline (https://hichip.readthedocs.io/en/latest/before_you_begin.html). Briefly, sequencing reads were first mapped to mm10 by bwa.[85] Then aligned results were processed by pairtools[86] to find ligation junctions in the HiChIP libraries, remove duplicates, and generate bam files for further analysis.

To prepare input files for loop calling, H3K27ac peaks were called by MACS2 for each replicate separately and interacting read pairs were extracted from the bam files. Loops were called by hichipper[73] for each replicate separately. Then filtered intra-chromosomal loops of all replicates by hichipper were pooled together into a union loop set. Read counts for the union loop set were extracted from 'one.interaction.bepe' file from hichipper. Significance of loops in the union set were calculated by mango.[74] Result files by mango were processed by diffloop[75] following the instruction of (https://rpubs.com/caleblareau/diffloop_vignette) to get the final filtered loop sets and normalized read counts. In the diffloop processing step, loops with mango_FDR larger than 0.01 were filtered out.The remaining loops with normalized read counts either in two E12.5 replicates or in two P42 replicates were kept as the final filtered loop set. Differential loops were defined as diffloop_fdr<0.05 and $|\log_2$ fold-change$| >= 2$.

ABC score

For each gene, the total ABC score[38] contributed by P300 enhancer was calculated using the formula below:

$$Total\ ABC\ score\ G\ =\ \sum_{k=1}^{n}(Ae_k * Ceg_k)$$

For gene G, n is the number of P300 enhancers within 5 Mb of the TSS of gene G, Ae_k is the Activity of P300 enhancer k (normalized enhancer signal in 400 bp window around enhancer peak), Ceg_k is the Hi-C contact between P300 enhancer k and the TSS of gene.

Fold change of total ABC score and gene expression of five adjacent genes ranked by fold change of gene expression calculated by DESeq2 were binned together. The fold-change from E12.5 to P42 was calculated as the ratio of the scores at P42 and E12.5. The correlation between fold change of total ABC score and fold change of gene expression was calculated using the Spearman method in R, using binned $\log_2$FC values.

For stage mis-matched ABC scores (Figure 6Giv), P42 and E12.5 contact data were swapped for calculation of ABC scores. For calculated, stage matched contact scores (Figure 6Gii), we used the genome-wide aggregate contact frequency as a function of distance (Figure 6H) in place of actual contact data. For calculated, stage mis-matched contact scores (Figure 6Giii), we swapped the contact frequency-distance relationship between E12.5 and P42.

HiChIP loops were used to analyze expression of genes linked to Early or Late P300 regions. Enhancer-promoter loops that overlapped Early or Late P300 regions linked these regions to genes. Linked genes were stratified by loop score quintile at E12.5 for Early P300, or at P42 for Late P300.

Super-enhancers

SE calling was performed using ROSE[87,88] on E12.5 and P42 P300 bioChIP-seq using default parameters. Stage specific and shared SEs were identified using bedtools[62] intersect. SE-associated genes were linked by H3K27ac HiChIP loops.

Please cite this article in press as: Zhou et al., Dynamic changes in P300 enhancers and enhancer-promoter contacts control mouse cardiomyocyte maturation, Developmental Cell (2023), https://doi.org/10.1016/j.devcel.2023.03.020

To calculate the aggregated interaction score of super-enhancers, typical P300 enhancers within super-enhancers were extracted by bedtools intersect. The interaction scores of all HiChIP loops with anchors overlapping these P300 enhancers were then summed to yield the aggregated super-enhancer interaction score.

Visualization of data with genome browser

ChIP-seq peaks were visualized with normalized RPKM value using IGV Genome Browser.[89] H3K27ac HiChIP data were visualized using WashU Epigenome Browser.[90] Average loop scores from two replicates for selected loops are labeled for comparison. For *Myh6-Myh7* and *Scn5a* loci, loops with scores under 15 were omitted for clarity.

QUANTIFICATION AND STATISTICAL ANALYSIS

Statistics

Statistical analysis was performed in Graphpad Prism or R. Bar graphs show mean ± SD, box plots show median, interquartile range, and the maximum and minimum values that are within 1.5 times the interquartile range of the 3rd and 1st quartile. Statistical tests are indicated in figure legends.